haematologica
Journal of the Ferrata Storti Foundation

NKX2-1 regulates cell survival, maturation, and DNA-damage responses as a cofactor of RUNX1 in T-cell acute lymphoblastic leukemia

by Linde Van Aerschot, Sofie Demeyer, Kalina Timcheva, Elien Heylen, Paulien Verstraete, Dylan De Groote, Marino Caruso, Lukas Lauwereins, Alexandra Veloso, Kim R. Kampen, Daniele Pepe, Nancy Boeckx, Jonathan Royaert, Jelle Verbeeck, Heidi Segers, Jan Cools, Kim De Keersmaecker and David Cabrerizo Granados

Received: April 8, 2025.
Accepted: December 24, 2025.

Citation: Linde Van Aerschot, Sofie Demeyer, Kalina Timcheva, Elien Heylen, Paulien Verstraete, Dylan De Groote, Marino Caruso, Lukas Lauwereins, Alexandra Veloso, Kim R. Kampen, Daniele Pepe, Nancy Boeckx,Jonathan Royaert, Jelle Verbeeck, Heidi Segers, Jan Cools, Kim De Keersmaecker and David Cabrerizo Granados. NKX2-1 regulates cell survival, maturation, and DNA-damage responses as a cofactor of RUNX1 in T-cell acute lymphoblastic leukemia.
Haematologica. 2026 Jan 8. doi: 10.3324/haematol.2025.287966 [Epub ahead of print]

Publisher's Disclaimer.
E-publishing ahead of print is increasingly important for the rapid dissemination of science. Haematologica is, therefore, E-publishing PDF files of an early version of manuscripts that have completed a regular peer review and have been accepted for publication.
E-publishing of this PDF file has been approved by the authors.
After having E-published Ahead of Print, manuscripts will then undergo technical and English editing, typesetting, proof correction and be presented for the authors' final approval; the final version of the manuscript will then appear in a regular issue of the journal.
All legal disclaimers that apply to the journal also pertain to this production process.

NKX2-1 regulates cell survival, maturation, and DNA-damage responses as a cofactor of RUNX1 in T-cell acute lymphoblastic leukemia

Linde van Aerschot[1,2], Sofie Demeyer[3,4], Kalina Timcheva[1,2], Elien Heylen[1,2,5], Paulien Verstraete[1,2], Dylan De Groote[1,2], Marino Caruso[1,2], Lukas Lauwereins[3,4], Alexandra Veloso[3,4], Kim R. Kampen[1,2,6], Daniele Pepe [1,2], Nancy Boeckx[7,8], Jonathan Royaert[1,2], Jelle Verbeeck[1,2], Heidi Segers,[9,10] Jan Cools[3,4], Kim De Keersmaecker[1,2#], David Cabrerizo Granados[1,2#]

[1] *Laboratory for Disease Mechanisms in Cancer, Department of Oncology, KU Leuven, Belgium.*
[2] *Laboratory for Disease Mechanisms in Cancer, Leuven Cancer Institute (LKI), Leuven, Belgium.*
[3] *Laboratory of Molecular Biology of Leukemia, Department of Human Genetics, KU Leuven, Belgium.*
[4] *Laboratory of Molecular Biology of Leukemia, Center for Cancer Biology, VIB, Leuven, Belgium.*
[5] *Centre for Tumour Microenvironment, Barts Cancer Institute, Queen Mary University of London, UK.*
[6] *Department of Radiation Oncology (MAASTRO), Maastricht University Medical Center, GROW School for Oncology and Reproduction, Maastricht, The Netherlands.*
[7] *Department of Laboratory Medicine, UZ Leuven, Belgium.*
[8] *Laboratory of Experimental Hematology, Department of Oncology, KU Leuven, Belgium.*
[9] *Paediatric Haematology and Oncology, University Hospitals Leuven, Leuven, Belgium.*
[10] *Department of Oncology / Pediatric Oncology, KU Leuven, Leuven, Belgium.*

[#] *DCG and KDK jointly supervised this work*

RUNNING TITLE: NKX2-1 in T-cell acute lymphoblastic leukemia

CORRESPONDING AUTHORS:

David Cabrerizo Granados (dcabrerizo-ibis@us.es*)*

Kim De Keersmaecker (kim.dekeersmaecker@kuleuven.be)

AUTHOR DISCLOSURES: No conflicts of interest to disclose.

DATA-SHARING STATEMENT: Data generated in this study are available within the article and its supplementary files. RNA-sequencing and ChIP-seq data are available on Gene Expression Omnibus (GEO) with accession numbers GSE288187 and GSE288188. Mass spectrometry data are available in PRIDE with identifiers PXD057622 and PXD057654.

ACKNOWLEDGEMENTS:

We thank the KU Leuven Genomics, FACS and flow cytometry and Bioimaging Leuven Core Facilities as well as our collaborators from Proteomics Leuven – Laboratory of Applied Mass Spectrometry (LAMaS) for their contribution to this work. For the analysis of RNA- and ChIP-sequencing samples, resources and services provided by the VSC (Flemish Supercomputer Center), funded by the Research Foundation – Flanders (FWO) and the Flemish Government, were used. We thank the lab of

Tom Taghon for kindly providing the OP9-hDLL4 cells used in this article, the lab of Geert Mortier for the RUNX1 overexpression plasmid, and Óscar Herranz for thorough proofreading of the manuscript.

FUNDING: This research was funded by grants from KU Leuven (C14/18/104), iBOF (iBOF/23/014), Kom op tegen Kanker (Emmanuel Van Der Schueren), Fonds Wetenschappelijk Onderzoek (FWO) (G0A4220N, G092620N) and by fundraising initiatives from VZW Baief. E.H. and P.V. received an FWO PhD fellowship fundamental research (1106121N and 1116822N), and A.V. was supported by a postdoctoral fellowship from FWO (12AZ324N).

CONTRIBUTIONS STATEMENT:

- Conception/Design of the work: LVA, KT, KDK and DCG
- Data collection: LVA, KT, DDG, EH, PV, MC, LL, AV, JR, JV, DCG
- Data analysis and interpretation: LVA, SD, KT, MC, DP, NB, HS, KRK, JC, KDK and DCG
- Drafting the article: LVA, KDK and DCG
- Critical revision of the article: all authors
- Final approval of the version to be published: KDK and DCG

ABSTRACT

T-cell acute lymphoblastic leukemia (T-ALL) is characterized by ectopic expression of transcription factors, including NKX2-1, which is overexpressed in 5% of patients. NKX2-1 is associated with a cortical immunophenotype and drives metabolic addiction to the serine/glycine synthesis pathway in T-ALL. However, a complete picture of the role of NKX2-1 in T-ALL pathogenesis is missing. We characterized a CRISPR-Cas9 NKX2-1 knockout model of RPMI-8402, the only known NKX2-1-expressing T-ALL cell line, and validated obtained results in patient samples. NKX2-1 knockout caused a less mature immunophenotype and promoted cell cycle progression, in line with direct transcriptional repression of CDK6 by NKX2-1 that we observed. Furthermore, NKX2-1 protected T-ALL cells from apoptosis and DNA damage. The NKX2-1 protein directly bound DNA repair factors, such as RPA1 and RPA2, and presence of NKX2-1 resulted in differential expression of gene sets related to DNA damage repair in RPMI-8402 cells and patient samples. Furthermore, NKX2-1 positive cells showed less induction of DNA damage and apoptosis upon treatment with etoposide, a DNA damaging chemotherapy agent that is clinically used to treat T-ALL. Mechanistically, our data supported that RUNX1 is an important co-factor for NKX2-1 transcriptional regulation in T-ALL cells, and that NKX2-1 modulated the composition of RUNX1 protein complexes. Notably, NKX2-1 expressing cells showed higher sensitivity towards RUNX1 inhibition, suggesting a cooperative role in regulating T-ALL cell survival. This work reveals a critical role of NKX2-1 in enhancing T-ALL cell survival through DNA damage protection, and identifies RUNX1 as an important cofactor in T-ALL pathogenesis.

MAIN TEXT

INTRODUCTION

T-cell acute lymphoblastic leukemia (T-ALL) arises by accumulation of somatic mutations that disrupt differentiation, proliferation, and survival of developing lymphocytes.[1] T-ALL cells typically harbor mutations that inactivate cell cycle regulators as CDKN2A/CDKN2B, as well as mutations that hyperactivate the NOTCH1 and PI3K/AKT or IL7R-JAK-STAT signaling pathways. This is often accompanied by alterations in epigenetic factors such as the EED, EZH2 and SUZ12 proteins of the polycomb repression complex 2 (PRC2), or protein translation factors such as mTOR, CNOT3, RPL10 or RPL22.[1–4] Furthermore, T-ALL patients can be classified into distinct transcriptional subgroups, by ectopic expression of a transcription factor such as TAL1, TLX1/3, HOXA, LMO1/2 or NKX2-1.[1]

While significant progress has been made on understanding the pathological processes in various T-ALL subgroups, less is known for the NKX2-1 subgroup.[5] NKX2-1 (also known as NKX2 homeobox 1) is a homeobox transcription factor with a critical role in development of the thyroid, lungs and ventral forebrain.[6] Loss of NKX2-1 expression is associated with pathologies affecting one or more of these organs, such as brain-thyroid-lung syndrome.[7] Moreover, aberrant NKX2-1 expression occurs in several cancer types. In lung adenocarcinoma (LUAD), 12% of patients display *NKX2-1* gene amplifications, with a higher prevalence in EGFR-positive cases where NKX2-1 acts as an oncogene through regulation of ROR1 and LMO3.[8–11] Conversely, NKX2-1 acts as tumor suppressor in $KRAS^{G12D}$ positive LUAD, resulting in loss of differentiation and enhanced tumor seeding activity by regulating genes implicated in cell-cell organization like claudin-18.[9,12] NKX2-1 is therefore known as a double-edged sword in LUAD, with its function heavily depending on genetic context. Moreover, NKX2-1 is overexpressed in 16% of neuroendocrine prostate cancers, driving reprogramming of prostate adenocarcinoma into the more aggressive neuroendocrine subtype.[13]

Although NKX2-1 is not expressed during normal T-cell development, ectopic NKX2-1 expression occurs in approximately 5% of T-ALL patients due to chromosomal rearrangements that juxtapose *NKX2-1* to the highly expressed T-cell receptor genes or due to *NKX2-1* gene amplifications. Transcriptional profiling of the NKX2-1 T-ALL subtype has revealed a proliferative gene expression signature, characterized by expression of cell cycle regulatory genes and a CD1a-positive immunophenotype, with cortical developmental arrest similar to the TLX1 subgroup.[5,14] Furthermore, we recently described the transcriptional induction of serine/glycine synthesis enzymes by NKX2-1 in T-ALL and LUAD, which leads to metabolic addiction to the serine/glycine synthesis pathway in NKX2-1-positive tumors.[15] However, a complete picture of the transcriptional targets of NKX2-1 in T-ALL is missing, and it remains unclear whether NKX2-1 plays additional roles in T-ALL development.

We generated an isogenic RPMI-8402 T-ALL NKX2-1 knockout model to investigate the role of NKX2-1 in T-ALL. We integrated NKX2-1 ChIP-seq, RNA-seq and IP-mass spectrometry datasets from this cell model and validated our findings in T-ALL patient samples **(Figure 1A)**. Our results demonstrate that NKX2-1 protects cells from apoptosis and DNA damage, conferring a lower sensitivity to etoposide, a clinically used DNA-damaging chemotherapeutic agent. Additionally, we identify RUNX1

as a cooperative co-factor of NKX2-1 in T-ALL cells, thereby shedding light on the role of NKX2-1 in T-ALL pathogenesis.

METHODS

Ethics

Genetic analysis and engineering of RPMI-8402 cells, as well as experiments on human patient derived xenograft (PDX) samples, were approved by the UZ Leuven ethical committee (S67079; S54608). Written informed consent was obtained from all patients or their parents, according to the Declaration of Helsinki.

CRISPR-Cas9

RPMI-8402 cells were electroporated (6 square wave pulses, 0.1 ms interval, 150 V) with a Cas9/GFP-encoding vector (pX458; Addgene) containing a sgRNA targeting NKX2-1 (5'-AAGATGTCAGACACTGAGAA-3'). After 48 h incubation in RPMI-1640 containing 10% Fetal Calf Serum (FCS), non-essential amino acids (Gibco) and 1 mM sodium pyruvate (Gibco), GFP-positive cells were sorted (BD FACS Aria III) and grown to single-cell derived colonies in ClonaCell-TCS (Stemcell Technologies), followed by expansion in liquid cultures in RPMI-1640 with 10% FCS. NKX2-1 knockout efficiency was evaluated by Synthego ICE analysis (v3.0) on Sanger sequencing results from genomic DNA of the targeted NKX2-1 locus.

RNA-sequencing

Total RNA was extracted from RPMI-8402 cells with the RNeasy kit (Qiagen) and was converted to 3' mRNA libraries with the QuantSeq library prep kit (Lexogen). Single-end, 50 bp reads were obtained on an Illumina HiSeq4000.

RNA-seq data from T-ALL patients were previously described.[16] The 40 samples with highest *NKX2-1* expression from the NKX2-1 subgroup were included for analysis, and compared to 40 random samples with no *NKX2-1* expression from the TAL1 subgroup.

Reads were mapped to the GENCODE human reference genome (GRCh38, v44) with STAR-aligner (v2.7.11a) and further processed using SAMtools (v1.18). Read counts per gene were obtained with FeatureCounts (Subread v2.0.3). Differential expression analysis was performed with the Limma R-package (v3.50.3) after removing low expressed genes using the FilterByExpression function in EdgeR (v3.36.0). Gene Set Enrichment Analysis was performed on ranked gene lists (GSEA v4.3.2, Broad Institute) with the ranking score calculated as -sign(log2 fold change)*log(adjusted p-value).[17,18] We conducted separate GSEAs for each database (KEGG, Reactome, Hallmarks, Gene Ontology). From these results, the final plots in our manuscript were obtained by performed a final GSEA on the pathways with strongest enrichment. The regulatory network was generated using iRegulon (v1.3) in Cytoscape (v3.8.2) on the significantly differentially expressed genes. Data were analyzed and visualized using RStudio (R v4.1.0). Sashimi plots were generated using ggsashimi v. 1.1.5.[19]

Immunoprecipitation

Protein extract from each RPMI-8402 NKX2-1$^{+/+}$ and NKX2-1$^{-/-}$ clone, or from PDX-XB14 was used for immunoprecipitation in cell lysis buffer (CST, #9803) supplemented with 5 mM Na_3VO_4 and cOmplete protease inhibitor (Roche). After pre-clearing BSA-blocked Protein G Magnetic Beads (Thermo Fisher Scientific, #88847) with rabbit IgG (CST, #2729) , immunoprecipitation was carried using 1µg of NKX2-1 (Abcam, #ab67820), 1µg (for IP) or 5µg (for IP-MS) of RUNX1 (Thermo Fisher Scientific, #PA-19638), 50-fold dilution of RPA1 (Cell Signaling Technology, #2267) or 0.5, 1 or 5µg IgG (CST, #2729) antibody. Samples were eluted in Novex Tris-Glycine SDS buffer supplemented with 5% β-mercaptoethanol, followed by western blotting or mass spectrometry analysis.

Statistics

Statistical analyses were performed in GraphPad Prism 10 using the statistical tests indicated in the figure legends.

Additional methods are in the supplementary file.

RESULTS

NKX2-1 promotes maturation and protects T-ALL cells from cell death and cell cycle progression

To identify a relevant model to investigate the role of NKX2-1 in T-ALL, we analyzed NKX2-1 mRNA and protein expression in a panel of 18 human T-ALL cell lines. Because RPMI-8402 was the only cell line expressing NKX2-1 (**Figure S1**),[20,21] these cells were CRISPR-Cas9 genome edited to generate isogenic NKX2-1 knockout cells (**Figure 1A**). Four single-cell-derived RPMI-8402 knockout clones, in which no residual NKX2-1 protein was detected on western blot, were chosen, along with four single-cell-derived wild-type control clones (further referred to as NKX2-1$^{-/-}$ and NKX2-1$^{+/+}$ clones, respectively) (**Figure 1B**).

To characterize the phenotype of knocking out NKX2-1 in RPMI-8402 cells, we first verified the immunophenotype of the obtained NKX2-1$^{+/+}$ and NKX2-1$^{-/-}$ clones. All clones were cyCD3^{+}/CD34^{+}/CD1a^{-}/CD5^{+}/CD7^{low}/CD2^{low} (**Figure S2A**), consistent with the described RPMI-8402 immunophenotype.[22] Remarkably, NKX2-1$^{+/+}$ clones showed a significant increase in CD2 and a decrease in CD34 mean fluorescent intensity, without altering the percentage of positive cells (**Figure 1C**). Moreover, whereas total CD45 levels were not affected by NKX2-1 knockout, NKX2-1$^{+/+}$ clones showed expression of lower molecular weight CD45 isoforms due to exon skipping **(Figure 1D-E, Figure S2B-D)**. These isoforms are a marker of T-cell differentiation status,[23] and further underscore the more differentiated T-cell phenotype in NKX2-1$^{+/+}$ cells.[24]

NKX2-1$^{+/+}$ clones displayed significantly less apoptotic cell death compared to NKX2-1$^{-/-}$ clones, as assessed by propidium iodide (PI), Annexin V, and cleaved caspase 3 stainings (**Figure 1F, Figure S3**). Interestingly, NKX2-1$^{+/+}$ clones also exhibited a higher percentage of cells in the G0-G1, and a lower percentage in the S-G2-M phases of the cell cycle (**Figure 1G**). Overall, these apoptosis and cell cycle phenotypes resulted in reaching similar cell densities for NKX2-1$^{+/+}$ and NKX2-1$^{-/-}$ clones over consecutive days (**Figure 1H**). Collectively, these findings suggest that NKX2-1 promotes a

slightly more mature immunophenotype, while also reducing apoptotic cell death and cell cycle progression in RPMI-8402 cells.

NKX2-1 is a transcriptional regulator of CDK6

To investigate the mechanistic role of NKX2-1, we performed NKX2-1 ChIP-seq on NKX2-1$^{+/+}$ clones, with NKX2-1$^{-/-}$ clones as negative controls. The majority of the 496 identified NKX2-1 binding peaks were located in intronic and distal intergenic regions, whereas 21% of the peaks were in promoter regions (**Figure 2A, Table S1**). Interestingly, we identified 25 genes with an adjacent NKX2-1 ChIP peak that were differentially expressed in RNA-sequencing (RNA-seq) on NKX2-1$^{+/+}$ versus NKX2-1$^{-/-}$ RPMI-8402 clones (**Figure S4**). Among the genes with NKX2-1 peaks, cyclin dependent kinase 6 (*CDK6*) was identified, essential for the progression from G1 to S phase in the cell cycle.[25] Furthermore, an open chromatin and enhancer region was observed in the same intronic area in public ATAC-seq and H3K27ac ChIP-seq data from RPMI-8402 cells, as well as a RUNX1 binding site (**Figure 2B**). Dual luciferase reporter assays in HEK-293T cells supported that NKX2-1 and RUNX1 are cooperatively regulating the activity of this *CDK6* enhancer region (**Figure S5**). Interestingly, CDK6 mRNA and protein levels were significantly reduced in NKX2-1$^{+/+}$ compared to NKX2-1$^{-/-}$ RPMI-8402 clones (**Figure 2C-E**). Altogether, these results support that NKX2-1 acts as a transcriptional regulator of CDK6, which is in line with the impaired cell cycle progression that we observed in NKX2-1$^{+/+}$ cells.

RNA-seq of NKX2-1 RPMI-8402 model reveals three clusters of differentially expressed gene sets

To further explore the role of NKX2-1 in T-ALL, we characterized the downstream effects of NKX2-1 by performing RNA-seq on our NKX2-1$^{+/+}$ versus NKX2-1$^{-/-}$ RPMI-8402 clones. Principal component analysis showed that the two analyzed genotypes formed separate clusters, and we identified 96 significantly differentially expressed genes (DEGs) (**Figure S6, Figure 3A**). Using Gene set enrichment analysis (GSEA), we confirmed enrichment of cell cycle-related pathways in the downregulated genes in NKX2-1$^{+/+}$ clones (**Figure 3B**). This GSEA revealed three additional major groups of gene sets regulated by NKX2-1, which were related to ribosome biology, epigenetics and DNA damage (**Figure 3C, Figure S7A**). As follow-up of these findings on ribosomal gene sets, we compared the functionality of ribosomes in NKX2-1$^{+/+}$ and NKX2-1$^{-/-}$ RPMI-8402 clones. However, no significant differences were observed in ribosomal polysome profiles or nascent protein synthesis levels (**Figure S7B-D**), suggesting that NKX2-1 does not substantially affect ribosomal function.

To further investigate the epigenetic gene set cluster identified in the GSEA (**Figure 3C**), we performed western blot analysis of several histone marks to examine the impact of NKX2-1 expression on the overall epigenetic landscape. NKX2-1$^{+/+}$ clones exhibited lower levels of H3K27ac, a marker of active chromatin, as well as reduced levels of H3K4me1 and H3K4me3, markers of active promoters and enhancers, respectively (**Figure 3D**). We hypothesized that the reduced histone mark levels in NKX2-1$^{+/+}$ clones may cause differential sensitivity to epigenetic drugs such as HDAC inhibitors (HDACi). Indeed, we observed a significantly decreased sensitivity of the NKX2-1$^{+/+}$ clones against the HDACi romidepsin and vorinostat (**Figure 3E**). This trend was confirmed in *ex vivo* cultured PDX samples exposed to romidepsin treatment, showing lower sensitivity on NKX2-1 positive samples (**Figure 3F,**

Figure S8). Therefore, we concluded that NKX2-1 reduces the levels of histone modifications in T-ALL, conferring the cells resistance to HDACi.

NKX2-1 protects T-ALL cells from DNA damage

Interestingly, DNA damage was also identified as a key cluster of differentially expressed gene sets in NKX2-1$^{+/+}$ versus NKX2-1$^{-/-}$ RPMI-8402 clones (**Figure 3C**). This led us to hypothesize that NKX2-1 may protect cells from DNA damage in T-ALL. To investigate this, we assessed the DNA damage status of the NKX2-1$^{+/+}$ and NKX2-1$^{-/-}$ clones by analyzing the γ-H2AX levels, a marker of DNA double strand breaks. NKX2-1$^{+/+}$ clones had significantly lower γ-H2AX levels compared to the NKX2-1$^{-/-}$ clones (**Figure 4A**). Additionally, we measured DNA damage markers H3K27me3, H3K56ac and H4K20me3 levels, and we observed the same reduction as for γ-H2AX in the NKX2-1$^{+/+}$ clones (**Figure 4A**).

Since DNA damage induction is often used as therapeutic strategy, we examined the impact of NKX2-1 expression on cellular sensitivity to etoposide, a clinically utilized DNA-damaging agent. As expected, following drug treatment, NKX2-1$^{+/+}$ clones demonstrated higher viability and lower levels of DNA damage markers γ-H2AX, H3K27me3 and olive moment in comet assays (**Figure 4B-D, Figure S9**). Also, for other clinically used DNA-damaging agents as doxorubicin and 6-thioguanine (6-TG), NKX2-1$^{+/+}$ clones showed a significantly higher IC50 value as compared to NKX2-1$^{-/-}$ cells (**Figure S10**). To corroborate these findings in patients, we analyzed public RNA-seq data of T-ALL patients by utilizing Pölönen *et al*.[16] We selected the 40 samples with highest NKX2-1 expression (NKX2-1 positive) as well as 40 samples lacking NKX2-1 expression belonging to the TAL1 subgroup (NKX2-1 negative). These TAL1 samples are an ideal control group, since these are not driven by a homeobox transcription factor but immunophenotypically resemble NKX2-1 positive T-ALL (**Figure S11**).[26] GSEA analysis on the RNA expression profiles of NKX2-1 positive versus negative samples revealed upregulated DNA damage repair pathways in the NKX2-1 positive group (**Figure 4E-F, Figure S12**). Interestingly, drug treatments on *ex vivo* cultured PDX samples also showed a trend towards more etoposide resistance in NKX2-1 positive samples (**Figure 4G, Figure S13**). Taken together, these findings support that NKX2-1 serves a protective role against DNA damage in T-ALL cells.

RUNX1 is a co-factor for transcriptional regulation by NKX2-1

To further elucidate the molecular mechanisms underlying NKX2-1 function in T-ALL cells, we identified NKX2-1 binding partners by immunoprecipitation (IP) of NKX2-1 in NKX2-1$^{+/+}$ RPMI-8402 cells, followed by mass spectrometry (MS) analysis, using NKX2-1$^{-/-}$ clones and IgG IP-MS as controls. Besides NKX2-1 itself, eight interacting proteins were identified (**Figure 5A**). Among these interactors, we identified RUNX Family Transcription Factor 1 (RUNX1), a critical hematopoietic transcription factor implicated in T-ALL.[22,27–29] We confirmed binding of NKX2-1 to RUNX1 by co-IP in our RPMI-8402 cell model and in an NKX2-1-positive PDX T-ALL sample (XB14) (**Figure 5B, Figure S14**).

In addition to the physical interaction between the NKX2-1 and RUNX1 proteins, our data suggested a cooperative role of RUNX1 and NKX2-1 in regulating gene expression in T-ALL. First, we used iRegulon to predict the transcriptional regulators of DEGs in the RNA-seq on the NKX2-1 RPMI-8402 cell model, identifying RUNX1 as a major regulator of these transcripts (**Figure 5C, Figure S15**).

Secondly, HOMER motif analysis of our NKX2-1 ChIP-seq data identified RUNX1 as one of the top-scoring motifs, alongside the NKX2 homeobox family (**Figure 5D, Table S2**). Besides confirming the specificity of our NKX2-1 ChIP-seq, this result suggests RUNX1 co-binding at NKX2-1 genomic binding sites. Finally, iRegulon analysis of public RNA-seq data from T-ALL patients confirmed RUNX1 as a key transcriptional regulator of DEGs in NKX2-1 positive versus negative samples, with an even higher normalized enrichment score (NES) than NKX2-1 itself (**Figure 5E, Figure S16**). Moreover, GSEA analysis indicated a significant positive enrichment of the Reactome pathway of RUNX1-regulated genes involved in the differentiation of hematopoietic stem cells (HSCs) in NKX2-1-positive patient samples (**Figure 5F**). Collectively, these data suggest that RUNX1 functions as co-factor of NKX2-1, working in close cooperation in the transcriptional regulation of T-ALL.

NKX2-1 modulates the binding partners of RUNX1 and cellular sensitivity to RUNX1 inhibition

To better understand the mechanistic interplay between NKX2-1 and RUNX1, we investigated the binding partners of RUNX1 in presence and absence of NKX2-1 by IP-MS in our RPMI-8402 cell clones (**Figure S17**). When comparing each condition to its corresponding IgG control, the majority (62%; 396/641) of identified RUNX1 binding partners were not affected by NKX2-1 status (**Figure 6A**). Furthermore, 18% of the RUNX1 protein partners in NKX2-1$^{+/+}$ clones were absent in NKX2-1$^{-/-}$ clones, with NKX2-1 itself being one of them. Conversely, 29% of the RUNX1 protein partners in NKX2-1$^{-/-}$ clones were exclusive to this condition (**Figure 6A**). These results suggest that whereas NKX2-1 affects a significant fraction of RUNX1 binding partners, the majority of RUNX1 interactors are insensitive to NKX2-1 presence.

When we compared the obtained RUNX1 interacting proteins to the previously identified NKX2-1 binding partners, we observed that all NKX2-1 interactors also bound RUNX1, except for Thymosin Beta 4 X-Linked (TMSB4X) (**Figure 6A**). Among these shared binding partners of NKX2-1 and RUNX1, we identified Replication Protein A1 and A2 (RPA1 and RPA2), which are involved in DNA damage recognition and nucleotide excision repair.[30] Given our previous results supporting a role for NKX2-1 in protecting cells from DNA damage, we validated by co-IP experiments that RPA1 binds NKX2-1 and RUNX1 in the NKX2-1 RPMI-8402 cell model and in NKX2-1-positive PDX samples (XB14) (**Figure S18**).

Next, we aimed to evaluate the cellular effects of RUNX1 inhibition. We tried to reduce RUNX1 expression with shRNAs. Unfortunately, RUNX1 knock-down was quickly lost in the cells, likely due to its toxicity, preventing us from performing the intended experiments. Therefore, we examined the effects of RUNX1 pharmacological inhibitor Ro5-3335.[31] We assessed our NKX2-1 RPMI-8402 clones over 5 days and observed a dose-dependent reduction in proliferation and increase in cell death (**Figure S19A-D**). By day 5, Ro5-3335 exhibited its most significant effect, causing similar levels of cell death at the highest drug concentrations irrespective of NKX2-1 status (**Figure 6B**). Interestingly, the kinetics of drug response was different at lower drug concentrations: whereas NKX2-1$^{+/+}$ cells started to respond (induction of PI-positive cells) from 2.5 µM of Ro5-3335 onwards, drug induced cell death only became apparent in NKX2-1$^{-/-}$ cells when a dose of 10 µM Ro5-3335 was applied (**Figure 6B**).

NKX2-1$^{+/+}$ cells were also sensitized to AI-10-47,[32] another pharmacological RUNX1 inhibitor (**Figure S19E**). This difference in drug sensitivity was also reflected in the accumulation of DNA damage, with NKX2-1$^{+/+}$ cells showing more Ro5-3335-induced DNA damage as compared to NKX2-1$^{-/-}$ cells in comet assays (**Figure 6C**). Finally, Ro5-3335 was also able to induce apoptosis in *ex vivo* cultured NKX2-1$^{+/+}$ T-ALL PDX samples (**Figure 6D-E, Figure S20**). Altogether, our results with RUNX1 inhibitor Ro5-3335 support that RUNX1 is essential for survival of T-ALL cells, irrespective of NKX2-1 status. However, the higher relative drug sensitivity of NKX2-1$^{+/+}$ cells, particularly with respect to DNA damage induction, suggests dependence of NKX2-1 on RUNX1 to execute its role in protecting T-ALL cells from DNA damage and cell death induction.

DISCUSSION

To better understand the role of NKX2-1 in T-ALL, we developed an isogenic cell model by knocking out NKX2-1 in the RPMI-8402 cell line. We opted for this model instead of overexpressing NKX2-1 in other T-ALL cell lines since their transcriptional programs are driven by other T-ALL-associated transcription factors, potentially confounding the results. Depletion of NKX2-1 in RPMI-8402 cells resulted in a slightly less mature phenotype, as evidenced by the differentiation-associated shifts in CD2 and CD34 expression. These changes suggest that NKX2-1 plays a role in maintaining a more differentiated T-cell state. Consistent with these results, our analysis of public RNA-seq data from T-ALL patients revealed that NKX2-1-positive tumors display upregulation of gene sets linked to HSC differentiation. Further underscoring this role in regulating T-cell differentiation, NKX2-1$^{+/+}$ clones expressed lower molecular weight CD45 isoforms. Interestingly, we found Heterogeneous Nuclear Ribonucleoprotein L Like (*HNRNPLL*), a gene showing NKX2-1 binding in our ChIP-seq, to be upregulated by NKX2-1 in our RNA-seq results **(Figure S4)**. This gene causes CD45 transcript exon-skipping, aligning with our results. In public patient data, we also observed a significant increase of *HNRNPL* (LogFC 0.45, adj.p value 0.00016), which has a similar activity as its paralog *HNRNPLL*.[33] We observed that NKX2-1 reduced apoptotic cell death over time, suggesting that NKX2-1 plays a role in supporting cell survival. In RPMI-8402 cells, we previously showed that NKX2-1 knockout increases ROS levels,[15] which may explain better survival of NKX2-1 positive cells. Our results are consistent with previous studies, which showed that NKX2-1 knockdown increases expression of apoptosis-related genes in LUAD and promotes apoptosis in small-cell lung cancer and neuroblasts.[34–36] However, other research has demonstrated that NKX2-1 can induce cell death through apoptosis in thyroid carcinoma cells.[37] This aligns with the previously suggested idea of NKX2-1 being a double-edged sword, supporting the notion that its effects may vary depending on the genetic context in which it is expressed.[10]

To decipher the chromatin binding areas of NKX2-1, we performed ChIP-seq on our RPMI-8402 model. Among the 496 detected peaks, one of them was in *CDK6*. Our data support that NKX2-1 regulates CDK6 at the transcriptional level. Interestingly, the same *CDK6* region where NKX2-1 binds coincided with a RUNX1 binding site (**Figure 2B**). Furthermore, our dual-luciferase reporter assays

show that NKX2-1 and RUNX1 are cooperatively modulating the activity of this CDK6 regulatory region (**Figure S5**), further underscoring the idea of RUNX1 and NKX2-1 being essential cofactors for transcriptional regulation in T-ALL. Previous studies have shown that NKX2-1 also inhibits CDK6 transcription in LUAD.[38] The observed CDK6 regulation by NKX2-1 may explain the reduction in cell cycle progression that we have observed in NKX2-1$^{+/+}$ clones. However, this regulation of CDK6 may also have indirect consequences for regulating the metabolism of NKX2-1 cells. Indeed, whereas we previously showed that NKX2-1 binds and transcriptionally induces the *de novo* serine and glycine synthesis pathway in T-ALL,[15] cyclin D3:CDK4/6 complex has also been identified as an indirect regulator of *de novo* serine and glycine synthesis in T-ALL.[39] Thus, our findings support the idea that NKX2-1 directly regulates CDK6 expression, driving cell cycle dysregulation and potentially also contributing to the NKX2-1-dependent induction of *de novo* serine/glycine synthesis addiction in T-ALL.

Further unraveling the role of NKX2-1 in T-ALL, GSEA on our RNA-seq data in the RPMI-8402 model identified three interesting clusters of enriched gene sets regulated by NKX2-1, including ribosomal gene sets. However, these detected transcriptional changes did not result in strong ribosomal phenotypes in the polysome profile or global protein synthesis. However, NKX2-1 knockout may modulate ribosomal function in a milder fashion, by leading to specialized ribosomes with more subtle altered translation phenotypes such as described for the RPL10 R98S mutation.[40,41] Furthermore, knocking out NKX2-1 may impact the extra-ribosomal functions of ribosomal proteins, which have been associated with tumorigenesis.[42,43] Interestingly, Liu *et al.* previously showed that mutations in ribosomal protein genes are highly enriched in NKX2-1 overexpression cases, suggesting a potential synergy.[26]

Another gene set cluster that was enriched in our NKX2-1 model was linked to epigenetics, confirmed by a differential amount of histone marks. Intriguingly, all histone modifications checked, both activating marks H3K27ac, H3K4me3 and H3K4me1, as well as repressive marks like H3K27me3, were strongly downregulated in the presence of NKX2-1. In line with this, NKX2-1 did not purely act as a repressor, or as an activator, and NKX2-1 ChIP-seq targets were induced or repressed (**Figure S4**). Interestingly, *HDAC4* was identified as a gene whose promoter region is bound by NKX2-1, resulting in transcriptional upregulation in NKX2-1$^{+/+}$ cells. This may explain the detected differences in histone acetylation. Furthermore, we previously showed that NKX2-1 regulates chromatin DNA and histone demethylases by modifying the ratio between succinate and alpha-ketoglutarate in lung cancer, which function as co-substrate of various histone demethylase enzymes.[15,44] From a therapeutic perspective, the downregulated histone marks in NKX2-1-driven T-ALL were associated with decreased sensitivity for HDACi like romidepsin and vorinostat, both clinically approved drugs that are investigated for treatment of T-ALL.[45–48]

Our observations related to the DNA damage protection function of NKX2-1 also have clinical relevance. Etoposide, doxorubicin and 6-TG are clinically used DNA-damaging agents to which NKX2-1-expressing cells showed reduced sensitivity.[49–51] NKX2-1 presence was associated with lower levels of γ-H2AX and reduced apoptosis, suggesting a role in minimizing DNA damage and promoting cell

survival. Interestingly, we also found that NKX2-1 binds to RPA1 and RPA2, proteins involved in DNA damage repair.[30] A role of NKX2-1 in DNA damage was already reported, as its overexpression was found to protect cells from DNA damage from DNA replication stress in LUAD by its binding with DDB1, a DNA damage response sensor protein found in UV-induced DNA lesions, and to RPA32.[52] In the context of LUAD and T-ALL, we also showed that NKX2-1 lowers ROS levels,[15] which may also add to the DNA damage protective role of NKX2-1.

Based on the NKX2-1 IP-MS results, we discovered that the transcription factor RUNX1 is a co-factor of NKX2-1. In addition to physical binding of these two proteins, our data also support a cooperative role in transcriptional regulation. HOMER motif analysis on the NKX2-1 ChIP-seq peaks identified RUNX1 motifs among the top-scoring motifs, and regulatory transcriptional network analysis on DEGs from RNA-seq of our RPMI-8402 model and from T-ALL patient data also showed RUNX1 as a top upstream transcription factor together with NKX family members, confirming a tight cooperation between these factors.

Given its different roles during hematopoiesis, RUNX1 is known to interact with other transcription factors and to recruit various co-factors to the chromatin. In this way, RUNX1 modifies the chromatin landscape and the transcriptional activity of its target genes. RUNX1 has been demonstrated to form a core transcriptional regulatory circuit in T-ALL with TAL1 and GATA3, as well as TLX1 and STAT5.[28,53] Here, we show that also NKX2-1 is one of the co-factors that cooperates with RUNX1, co-regulating expression of gene sets crucial for T-ALL tumorigenesis.[22] Additionally, the greater sensitivity of NKX2-$1^{+/+}$ clones to RUNX1 inhibition reinforces the importance of NKX2-1 in supporting the cellular mechanisms orchestrated by RUNX1, thus emphasizing their interdependent roles in T-ALL progression. Given the importance of RUNX1 in hematopoiesis, and its known functions independent of NKX2-1, it is not surprising that also NKX2-1 negative T-ALL cell lines display RUNX1 inhibitor sensitivity (**Figure S21**), and targeting of RUNX1 for therapeutic purposes may come with a limited therapeutic window.

In conclusion, the findings in this study (summarized in **Figure 6F)** highlight the critical role of NKX2-1 in regulating T-ALL maturation state, protecting cells from apoptosis and altering their cell cycle progression. Moreover, NKX2-1 confers resistance to DNA damage and HDACi. We analyzed the binding partners of NKX2-1 and found a novel tight relationship with RUNX1 in cooperatively driving the T-ALL transcriptional network.

REFERENCES

1. Girardi T, Vicente C, Cools J, De Keersmaecker K. The genetics and molecular biology of T-ALL. Blood. 2017;129(9):1113-1123.
2. De Keersmaecker K, Atak ZK, Li N, et al. Exome sequencing identifies mutation in CNOT3 and ribosomal genes RPL5 and RPL10 in T-cell acute lymphoblastic leukemia. Nat Genet. 2013;45(2):186-190.
3. Tran TH, Hunger SP. The genomic landscape of pediatric acute lymphoblastic leukemia and precision medicine opportunities. Semin Cancer Biol. 2022;84:144-152.
4. Brady SW, Roberts KG, Gu Z, et al. The genomic landscape of pediatric acute lymphoblastic leukemia. Nat Genet. 2022;54(9):1376-1389.
5. Homminga I, Pieters R, Langerak AW, et al. Integrated Transcript and Genome Analyses Reveal NKX2-1 and MEF2C as Potential Oncogenes in T Cell Acute Lymphoblastic Leukemia. Cancer Cell. 2011;19(4):484-497.
6. Lazzaro D, Price M, de Felice M, Di Lauro R. The transcription factor TTF-1 is expressed at the onset of thyroid and lung morphogenesis and in restricted regions of the foetal brain. Development. 1991;113(4):1093-1104.
7. Willemsen MAAP, Breedveld GJ, Wouda S, et al. Brain-Thyroid-Lung syndrome: a patient with a severe multi-system disorder due to a de novo mutation in the thyroid transcription factor 1 gene. Eur J Pediatr. 2005;164(1):28-30.
8. Weir BA, Woo MS, Getz G, et al. Characterizing the cancer genome in lung adenocarcinoma. Nature. 2007;450(7171):893-898.
9. Yamaguchi T, Hosono Y, Yanagisawa K, Takahashi T. NKX2-1/TTF-1: An Enigmatic Oncogene that Functions as a Double-Edged Sword for Cancer Cell Survival and Progression. Cancer Cell. 2013;23(6):718-723.
10. Yamaguchi T, Yanagisawa K, Sugiyama R, et al. NKX2-1/TITF1/TTF-1-Induced ROR1 Is Required to Sustain EGFR Survival Signaling in Lung Adenocarcinoma. Cancer Cell. 2012;21(3):348-361.
11. Watanabe H, Francis JM, Woo MS, et al. Integrated cistromic and expression analysis of amplified NKX2-1 in lu ng adenocarcinoma identifies LMO3 as a functional transcriptional target. Genes Dev. 2013;27(2):197-210.
12. Niimi T, Nagashima K, Ward JM, et al. claudin-18, a Novel Downstream Target Gene for the T/EBP/NKX2.1 Homeodomain Transcription Factor, Encodes Lung- and Stomach-Specific Isoforms through Alternative Splicing. Mol Cell Biol. 2001;21(21):7380-7390.
13. Baca SC, Takeda DY, Seo J-H, et al. Reprogramming of the FOXA1 cistrome in treatment-emergent neuroendocrine prostate cancer. Nat Commun. 2021;12(1):1979.
14. Ferrando AA, Neuberg DS, Staunton J, et al. Gene expression signatures define novel oncogenic pathways in T cell acute lymphoblastic leukemia. Cancer Cell. 2002;1(1):75-87.
15. Heylen E, Verstraete P, Van Aerschot L, et al. Transcription factor NKX2-1 drives serine and glycine synthesis addiction in cancer. Br J Cancer. 2023;128(10):1862-1878.

16. Pölönen P, Di Giacomo D, Seffernick AE, et al. The genomic basis of childhood T-lineage acute lymphoblastic leukaemia. Nature. 2024;632(8027):1082-1091.

17. Mootha VK, Lindgren CM, Eriksson K-F, et al. PGC-1α-responsive genes involved in oxidative phosphorylation are coordinately downregulated in human diabetes. Nat Genet. 2003;34(3):267-273.

18. Subramanian A, Tamayo P, Mootha VK, et al. Gene set enrichment analysis: A knowledge-based approach for interpreting genome-wide expression profiles. Proc Natl Acad Sci U S A. 2005;102(43):15545-15550.

19. Garrido-Martín D, Palumbo E, Guigó R, Breschi A. ggsashimi: Sashimi plot revised for browser- and annotation-independent splicing visualization. PLoS Comput Biol 2018;14(8):e1006360.

20. Quentmeier H, Pommerenke C, Dirks WG, et al. The LL-100 panel: 100 cell lines for blood cancer studies. Sci Rep. 2019;9(1):114.

21. Kalender Atak Z, Gianfelici V, Hulselmans G, et al. Comprehensive Analysis of Transcriptome Variation Uncovers Known and Novel Driver Events in T-Cell Acute Lymphoblastic Leukemia. PLoS Genet. 2013;9(12):e1003997.

22. Sanda T. RUNX1 in T-ALL: tumor suppressive or oncogenic? Blood. 2017;130(15):1686-1688.

23. Rheinländer A, Schraven B, Bommhardt U. CD45 in human physiology and clinical medicine. Immunol Let. 2018;196:22-32.

24. Dawes R, Petrova S, Liu Z, Wraith D, Beverley PCL, Tchilian EZ. Combinations of CD45 Isoforms Are Crucial for Immune Function and Disease. J Immunol. 2006;176(6):3417-3425.

25. Morgan DO. Cyclin-dependent kinases: Engines, Clocks, and Microprocessors. Annu Rev Cell Dev Biol. 1997;13(1):261-291.

26. Liu Y, Easton J, Shao Y, et al. The genomic landscape of pediatric and young adult T-lineage acute lymphoblastic leukemia. Nat Genet. 2017;49(8):1211-1218.

27. Choi Ah, Illendula A, Pulikkan JA, et al. RUNX1 is required for oncogenic Myb and Myc enhancer activity in T-cell acute lymphoblastic leukemia. Blood. 2017;130(15):1722-1733.

28. Sanda T, Lawton LN, Barrasa MI, et al. Core Transcriptional Regulatory Circuit Controlled by the TAL1 Complex in Human T Cell Acute Lymphoblastic Leukemia. Cancer Cell. 2012;22(2):209-221.

29. Della Gatta G, Palomero T, Perez-Garcia A, et al. Reverse engineering of TLX oncogenic transcriptional networks identifies RUNX1 as tumor suppressor in T-ALL. Nat Med. 2012;18(3):436-440.

30. He Z, Henricksen LA, Wold MS, Ingles CJ. RPA involvement in the damage-recognition and incision steps of nucleotide excision repair. Nature. 1995;374(6522):566-569.

31. Cunningham L, Finckbeiner S, Hyde RK, et al. Identification of benzodiazepine Ro5-3335 as an inhibitor of CBF leukemia through quantitative high throughput screen

against RUNX1-CBFβ interaction. Proc Natl Acad Sci U S A. 2012;109(36):14592-14597.

32. Illendula A, Gilmour J, Grembecka J, et al. Small Molecule Inhibitor of CBFβ-RUNX Binding for RUNX Transcription Factor Driven Cancers. EBioMedicine. 2016;8:117-131.

33. Preußner M, Schreiner S, Hung L-H, et al. HnRNP L and L-like cooperate in multiple-exon regulation of CD45 alternative splicing. Nucleic Acids Res. 2012;40(12):5666-5678.

34. Isogaya K, Koinuma D, Tsutsumi S, et al. A Smad3 and TTF-1/NKX2-1 complex regulates Smad4-independent gene expression. Cell Res. 2014;24(8):994-1008.

35. Kong R, Patel AS, Sato T, et al. Transcriptional Circuitry of NKX2-1 and SOX1 Defines an Unrecognized Lineage Subtype of Small-Cell Lung Cancer. Am J Respir Crit Care Med. 2022;206(12):1480-1494.

36. Jia S, Zhang L, Zhang K, et al. Nkx2.1 downregulation is involved in brain abnormality induced by excess retinoic acid. Acta Biochim Biophys Sin (Shanghai) 2020;52(6):683-690.

37. Ito Y, Furuya F, Taki K, Suzuki H, Shimura H. NKX2-1 re-expression induces cell death through apoptosis and necrosis in dedifferentiated thyroid carcinoma cells. PLoS One. 2021;16(11):e0259558.

38. Maeda Y, Tsuchiya T, Hao H, et al. KrasG12D and Nkx2-1 haploinsufficiency induce mucinous adenocarcinoma of the lung. J Clin Invest. 2012;122(12):43884400.

39. Wang H, Nicolay BN, Chick JM, et al. The metabolic function of cyclin D3-CDK6 kinase in cancer cell survival. Nature. 2017;546(7658):426430.

40. Kampen KR, Fancello L, Girardi T, et al. Translatome analysis reveals altered serine and glycine metabolism in T-cell acute lymphoblastic leukemia cells. Nat Commun. 2019;10(1):2542.

41. Caruso M, De Keersmaecker K. Ribosome specialization by cancer-associated ribosomal protein mutations: progress made and open questions. Philo Trans R Soc Lond B Biol Sci. 2025;380(1921):20230380.

42. Sulima SO, Hofman IJF, De Keersmaecker K, Dinman JD. How Ribosomes Translate Cancer. Cancer Discov. 2017;7(10):1069-1087.

43. Sulima SO, Kampen KR, Vereecke S, et al. Ribosomal Lesions Promote Oncogenic Mutagenesis. Cancer Res. 2019;79(2):320-327.

44. Tran TQ, Lowman XH, Kong M. Molecular Pathways: Metabolic Control of Histone Methylation and Gene Expression in Cancer. Clin Cancer Res. 2017;23(15):4004-4009.

45. Brunvand MW, Carson J. Complete remission with romidepsin in a patient with T-cell acute lymphoblastic leukemia refractory to induction hyper-CVAD. Hematol Oncol. 2018;36(1):340-343.

46. Song Y, Chen S, Liu C, et al. Chemo-free maintenance therapy in adult T-cell acute lymphoblastic leukemia: A case report and literature review. Front Pharmacol. 2023;14:1051305.

47. Burke MJ, Lamba JK, Pounds S, et al. A therapeutic trial of decitabine and vorinostat in combination with chemotherapy for relapsed/refractory acute lymphoblastic leukemia. Am J Hematol. 2014;89(9):889-895.

48. Burke MJ, Kostadinov R, Sposto R, et al. Decitabine and Vorinostat with Chemotherapy in Relapsed Pediatric Acute Lymphoblastic Leukemia: A TACL Pilot Study. Clin Cancer Res. 2020;26(10):2297-2307.

49. Whitlock JA, Malvar J, Dalla-Pozza L, et al. Nelarabine, etoposide, and cyclophosphamide in relapsed pediatric T-acute lymphoblastic leukemia and T-lymphoblastic lymphoma (study T2008-002 NECTAR). Pediatr Blood Cancer. 2022;69(11):e29901.

50. Escherich G, Zimmermann M, Janka-Schaub G. Doxorubicin or daunorubicin given upfront in a therapeutic window are equally effective in children with newly diagnosed acute lymphoblastic leukemia. A randomized comparison in trial CoALL 07-03. Pediatr Blood Cancer. 2013;60(2):254-257.

51. Toksvang LN, Als-Nielsen B, Bacon C, et al. Thiopurine Enhanced ALL Maintenance (TEAM): study protocol for a randomized study to evaluate the improvement in disease-free survival by adding very low dose 6-thioguanine to 6-mercaptopurine/methotrexate-based maintenance therapy in pediatric and adult patients (0–45 years) with newly diagnosed B-cell precursor or T-cell acute lymphoblastic leukemia treated according to the intermediate risk-high group of the ALLTogether1 protocol. BMC Cancer. 2022;22(1):483.

52. Liu Z, Yanagisawa K, Griesing S, et al. TTF-1/NKX2-1 binds to DDB1 and confers replication stress resistance to lung adenocarcinomas. Oncogene. 2017;36(26):3740-3748.

53. Vanden Bempt M, Demeyer S, Broux M, et al. Cooperative Enhancer Activation by TLX1 and STAT5 Drives Development of NUP214-ABL1/TLX1-Positive T Cell Acute Lymphoblastic Leukemia. Cancer Cell. 2018;34(2):271-285.e7.

FIGURE LEGENDS

Figure 1. **Phenotypic characterization of NKX2-1 in RPMI-8402 cells. (A)** Schematic workflow of the study illustrating the NKX2-1 RPMI-8402 knockout model generation, the experiments performed on this model, and confirmation in patient samples. **(B)** Immunoblot analysis of NKX2-1 in NKX2-1$^{+/+}$ and NKX2-1$^{-/-}$ CRISPR-Cas9 clones used in this project. The NKX2-1 specific signal is indicated with an arrow. The band at 37 kDa is a nonspecific signal. Histone 3 (H3) served as loading control. **(C)** Mean Fluorescence Intensity (MFI) quantification of CD45^{+} cells based on flow cytometry data of cyCD3, CD5, CD34, CD2, CD7 and CD1a. Data are represented as mean ± SD of four clones per genotype. Dots indicate values obtained from individual clones. Statistics were calculated by an unpaired two-tailed t-test. **(D)** Immunoblot analysis of CD45 in NKX2-1$^{+/+}$ and NKX2-1$^{-/-}$ RPMI-8402 clones. Lamin B1 served as loading control. **(E)** Sashimi plot based on RNA-seq data illustrating differential splicing of *PTPRC* with exon skipping in NKX2-1$^{-/-}$ RPMI-8402 clones. The plot shows data from one representative clone per genotype. A threshold of minimum 20 junction reads was applied. **(F)** Percentage of Propidium Iodide (PI)-positive cells detected by flow cytometry in NKX2-1$^{+/+}$ and NKX2-1$^{-/-}$ RPMI-8402 clones at day 5. Data are represented as mean ± SD of four clones per genotype. Dots indicate values obtained from individual clones. Statistics were calculated by an unpaired two-tailed t-test. **(G)** Left: Representative cell cycle profiles of NKX2-1$^{+/+}$ and NKX2-1$^{-/-}$ RPMI-8402 clones using PI staining in flow cytometry. Right: Quantification of G0-G1 and S-G2-M phases at day 5. Data are represented as mean ± SD of four clones per genotype. Dots indicate values obtained from individual clones. Statistics were calculated by an unpaired two-tailed t-test. **(H)** Proliferation curve of NKX2-1$^{+/+}$ and NKX2-1$^{-/-}$ RPMI-8402 clones. The plotted relative viable cell numbers were determined by PI flow cytometry. Data are represented as mean ± SD of four clones per genotype. *p-value < 0.05, **p-value < 0.01.

Figure 2. NKX2-1 directly represses CDK6 expression. (A) Peak distribution of NKX2-1 ChIP-seq in NKX2-1$^{+/+}$ RPMI-8402 cells as defined by ChIPseeker. **(B)** Genomic locus of the *CDK6* gene with NKX2-1 ChIP-seq peak, H3K27ac ChIP-seq and ATAC-seq signal in RPMI-8402 cells, and RUNX1 ChIP-seq peaks from 22 hematopoietic cell models obtained from chip-atlas.org. **(C)** Quantification of CDK6 mRNA expression by RT-qPCR in NKX2-1$^{+/+}$ and NKX2-1$^{-/-}$ RPMI-8402 clones at day 5. Individual dots represent 4 biologically independent clones per genotype. Data are represented as mean ± SD, statistics were calculated by an unpaired two-tailed t-test. **(D)** Immunoblot analysis of CDK6 in the NKX2-1$^{+/+}$ and NKX2-1$^{-/-}$ RPMI-8402 clones. Vinculin served as loading control. **(E)** Fold change of CDK6 protein expression densitometry of western blots from three independent experiments on NKX2-1$^{+/+}$ and NKX2-1$^{-/-}$ RPMI-8402 clones at day 5. Data are represented as mean ± SEM, statistics were calculated by two-way ANOVA. *p-value < 0.05.

Figure 3. RNA-sequencing of NKX2-1$^{+/+}$ and NKX2-1$^{-/-}$ RPMI-8402 clones reveals differentially expressed gene sets related to DNA damage and epigenetics, altering the epigenetic landscape and sensitivity towards HDAC inhibitors. (A) Volcano plot showing differentially expressed genes detected by RNA-seq analysis of NKX2-1$^{+/+}$ and NKX2-1$^{-/-}$ RPMI-8402 clones (4 clones per genotype). The grey dotted lines indicate the cut-off values for significance (adj.P.Val<0.05) and fold change

(FC>2). **(B)** GSEA enrichment plots showing downregulation of cell cycle-related gene sets in NKX2-1$^{+/+}$ RPMI-8402 cells. **(C)** GSEA dot plot showing the top enriched gene sets belonging to the DNA damage and epigenetic cluster in the NKX2-1$^{+/+}$ RPMI-8402 model. **(D)** Immunoblots of H3K27ac, H3K4me1 and H3K4me3 in NKX2-1$^{+/+}$ and NKX2-1$^{-/-}$ RPMI-8402 clones. Lamin B1 served as loading control. **(E)** Dose-response curves of NKX2-1$^{+/+}$ and NKX2-1$^{-/-}$ RPMI-8402 clones treated for 48 h with romidepsin (left) or vorinostat (right). Data points represent mean ± SD of relative proliferation of 4 biologically independent clones per genotype, normalized to day 0 and DMSO vehicle condition. Least-squares regression fits to the mean are shown (solid lines), and IC50 values were determined for each drug and condition. Statistics were calculated by an extra sum-of-squares F-test. **(F)** Relative cell death of NKX2-1-positive and -negative PDX samples after treatment for 72 h with romidepsin. Data were normalized to DMSO vehicle treated cells. Data are represented as mean ± SD, statistics were calculated by an unpaired two-tailed t-test. **p-value < 0.01.

Figure 4. NKX2-1 protects cells against DNA damage. (A) Top: Immunoblot analysis of γ-H2AX and H3K27me3 in NKX2-1$^{+/+}$ and NKX2-1$^{-/-}$ RPMI-8402 clones. Vinculin served as loading control. Bottom: Immunoblot analysis of H3K56ac and H4K20me3 in NKX2-1$^{+/+}$ and NKX2-1$^{-/-}$ RPMI-8402 clones. Lamin B1 served as loading control. **(B)** Dose-response curves of NKX2-1$^{+/+}$ and NKX2-1$^{-/-}$ RPMI-8402 clones treated for 48 h with etoposide. Data points represent mean ± SD of relative proliferation of four clones per genotype, normalized to Day 0 and DMSO vehicle condition. Least-squares regression fits to the mean are shown (solid lines), and IC50 values were determined. Statistics were calculated by an extra sum-of-squares F-test. **(C)** Immunoblot for γ-H2AX and H3K27me3 (short and long exposure) in NKX2-1$^{+/+}$ and NKX2-1$^{-/-}$ RPMI-8402 samples (mix of four clones per genotype) after treatment with 200 nM etoposide for 48 h. Vinculin served as loading control. **(D)** Left: Olive moment in comet assay on NKX2-1$^{+/+}$ and NKX2-1$^{-/-}$ RPMI-8402 cells after 48 h of treatment with 200 nM etoposide. Data represented as mean ± SEM, statistics were calculated by a Mann-Whitney two-tailed test. Right: Representative comet stained with PI obtained from NKX2-1$^{+/+}$ and NKX2-1$^{-/-}$ RPMI-8402 cells after 48 h of treatment with 200 nM etoposide. **(E)** Dot plot showing enriched gene sets linked to DNA damage repair identified in the GSEA of differentially expressed genes in NKX2-1-positive versus negative T-ALL patient data from Pölönen *et al*.[16] **(F)** GSEA enrichment plots showing upregulation of DNA repair gene sets in NKX2-1-positive T-ALL patients. **(G)** Relative cell death of NKX2-1-positive and -negative PDX samples after treatment for 72 h with 1 µM etoposide. Data are normalized to DMSO vehicle treated cells. Data are represented as mean ± SD, statistics were calculated by an unpaired two-tailed t-test. **p-value < 0.01. ***p-value < 0.001.

Figure 5. RUNX1 is a co-factor of NXK2-1. (A) Volcano plot showing differentially detected NKX2-1 binding proteins by IP-MS in NKX2-1$^{+/+}$ compared to NKX2-1$^{-/-}$ RPMI-8402 clones and IgG IP. Four clones per genotype were analyzed. The grey dotted lines indicate the cut-off values for significance (qvalue<0.1) and fold change (FC>2). **(B)** Immunoblot for NKX2-1, RUNX1 and histone 3 (H3) of input, IgG control and RUNX1 immunoprecipitated samples of NKX2-1$^{+/+}$ or NKX2-1$^{-/-}$ RPMI-8402 cells (mix of four clones per genotype) (left) or NKX2-1 positive PDX XB14 sample (right). **(C)** iRegulon analysis on significantly DEGs in NKX2-1$^{+/+}$ RPMI-8402 clones compared to NKX2-1$^{-/-}$ clones. NKX6-3 was

identified as top-scoring motif for the NKX family, but has high similarity to NKX2-1. NES values for each cluster code are shown from each transcription factor. DEGs are colored according to their logFC. **(D)** Representative motifs from two top-scoring motif families, ranked on p-value, identified by HOMER motif enrichment analysis on NKX2-1 ChIP-seq from NKX2-1$^{+/+}$ clones. **(E)** iRegulon analysis on top 10% significantly DEGs in NKX2-1-positive compared to NKX2-1-negative T-ALL samples. Predicted transcription factors are indicated in orange and blue octagons. NES values for each cluster code are shown for each transcription factor. DEGs are colored according to their logFC. **(F)** GSEA enrichment plot showing upregulation of RUNX1-regulated genes involved in HSC differentiation in NKX2-1-positive T-ALL patients.

Figure 6. NKX2-1 alters RUNX1 binding partners and modulates sensitivity to RUNX1 inhibition. **(A)** Venn diagram illustrating significantly bound proteins to RUNX1 in NKX2-1$^{+/+}$ (light blue) or NKX2-1$^{-/-}$ (purple) RPMI-8402 clones and to NKX2-1 in NKX2-1$^{+/+}$ clones (orange). **(B)** Percentage of PI-positive dead cells detected by flow cytometry in NKX2-1$^{+/+}$ and NKX2-1$^{-/-}$ RPMI-8402 cells after treatment with Ro5-3335 for 5 days. Data represented as mean ± SD, statistics calculated by an ordinary one-way ANOVA followed by a Tukey's HSD post hoc test. **(C)** Left: Olive moment measured in comet assays on NKX2-1$^{+/+}$ and NKX2-1 $^{-/-}$ RPMI-8402 cells after 5 days of treatment with 50 µM Ro5-3335. Data represented as mean ± SEM, statistics calculated by Mann-Whitney two-tailed test. Right: Representative comet stained with PI from NKX2-1$^{+/+}$ and NKX2-1 $^{-/-}$ RPMI-8402 cells after 5 days of treatment with 50 µM Ro5-3335. (**D)** Effect of treatment of NKX2-1 positive PDX XB41 with 50 µM Ro5-3335 or DMSO vehicle. Left: Relative proliferation of treated cells normalized to Day 0. Right: Absolute percentage of dead cells, identified as PI-positive cells by flow cytometry. Individual dots represent 3 technical replicates. Data represented as mean ± SD, statistics calculated by two-way ANOVA followed by a Šidák test. **(E)** Flow cytometry analysis of cleaved caspase 3/Zombie Aqua of XB47 NKX2-1 positive PDX cells after 72 h of treatment with DMSO vehicle or 50 µM Ro5-3335. **(F)** Proposed model of the role of NKX2-1 in T-ALL (Created with Servier Medical Art released under the Creative Commons Attribution 4.0 International License). *p-value < 0.05, **p-value < 0.01, ***p-value < 0.001. p-values were calculated using a two-tailed t-test.

Figure 1

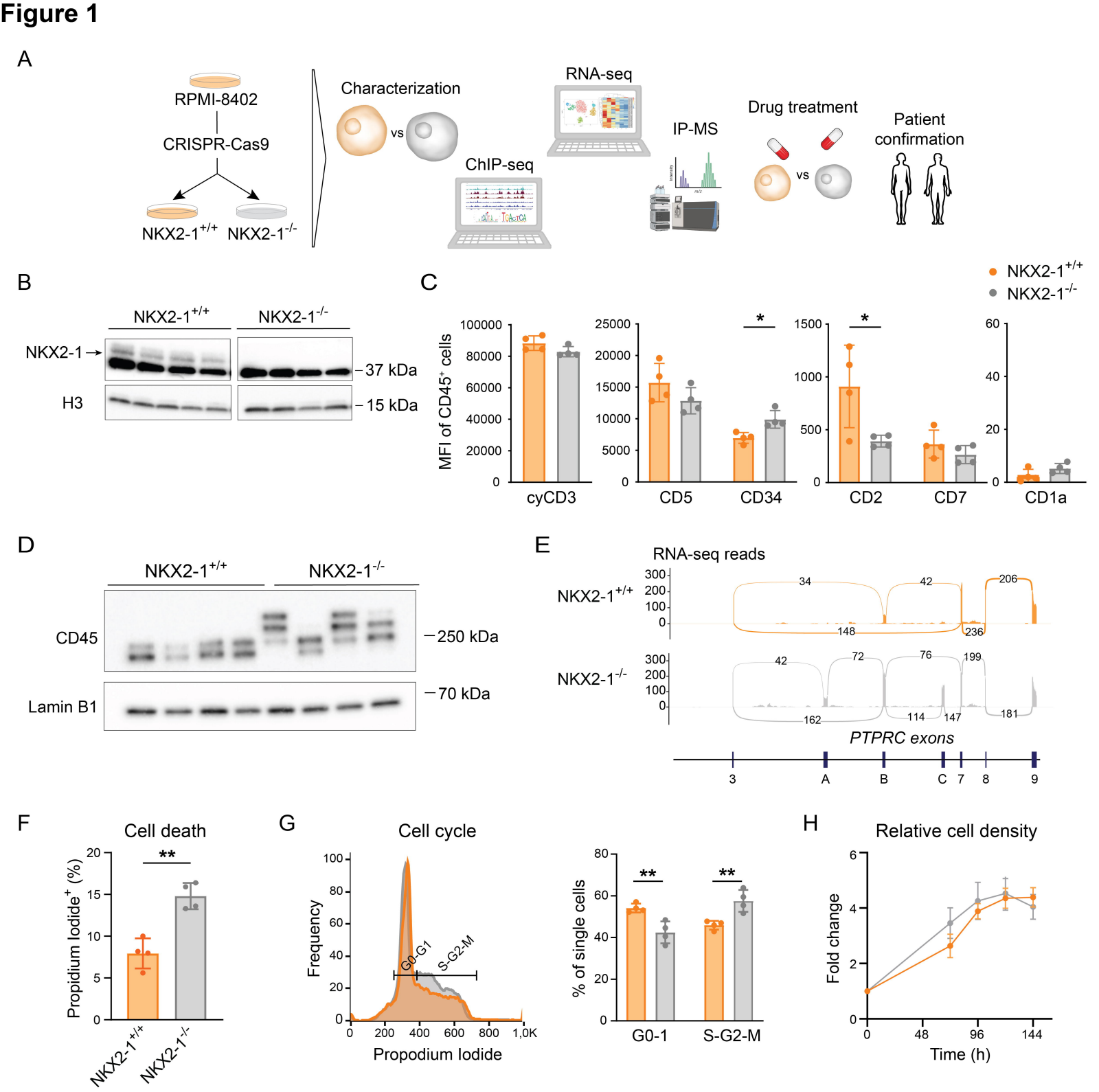
A
RPMI-8402
CRISPR-Cas9
NKX2-1+/+
NKX2-1-/-
Characterization
vs
ChIP-seq
RNA-seq
IP-MS
Drug treatment
vs
Patient confirmation
B
NKX2-1+/+
NKX2-1-/-
NKX2-1
H3
37 kDa
15 kDa
C
NKX2-1+/+
NKX2-1-/-
MFI of CD45+ cells
cyCD3
CD5
CD34
CD2
CD7
CD1a
D
NKX2-1+/+
NKX2-1-/-
CD45
Lamin B1
250 kDa
70 kDa
E
RNA-seq reads
NKX2-1+/+
NKX2-1-/-
PTPRC exons
F
Cell death
Propidium Iodide+ (%)
NKX2-1+/+
NKX2-1-/-
G
Cell cycle
Frequency
G0-G1
S-G2-M
Propodium Iodide
% of single cells
G0-1
S-G2-M
H
Relative cell density
Fold change
Time (h)

Figure 2

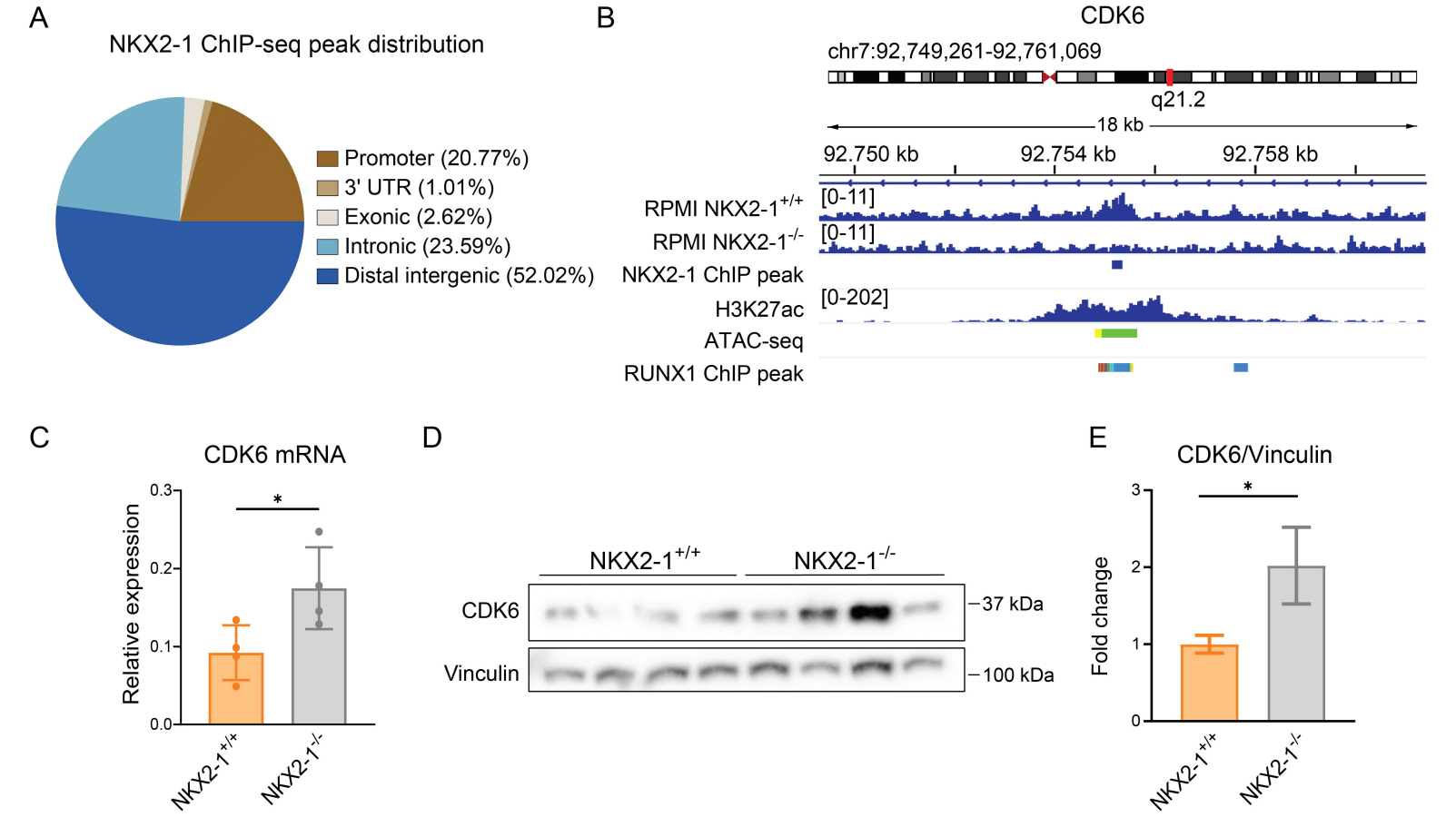
A
NKX2-1 ChIP-seq peak distribution
Promoter (20.77%)
3' UTR (1.01%)
Exonic (2.62%)
Intronic (23.59%)
Distal intergenic (52.02%)
B
CDK6
chr7:92,749,261-92,761,069
q21.2
18 kb
92.750 kb
92.754 kb
92.758 kb
RPMI NKX2-1+/+
RPMI NKX2-1-/-
NKX2-1 ChIP peak
H3K27ac
ATAC-seq
RUNX1 ChIP peak
[0-11]
[0-11]
[0-202]
C
CDK6 mRNA
Relative expression
0.3
0.2
0.1
0.0
*
NKX2-1+/+
NKX2-1-/-
D
NKX2-1+/+
NKX2-1-/-
CDK6
Vinculin
37 kDa
100 kDa
E
CDK6/Vinculin
Fold change
3
2
1
0
*
NKX2-1+/+
NKX2-1-/-

Figure 3

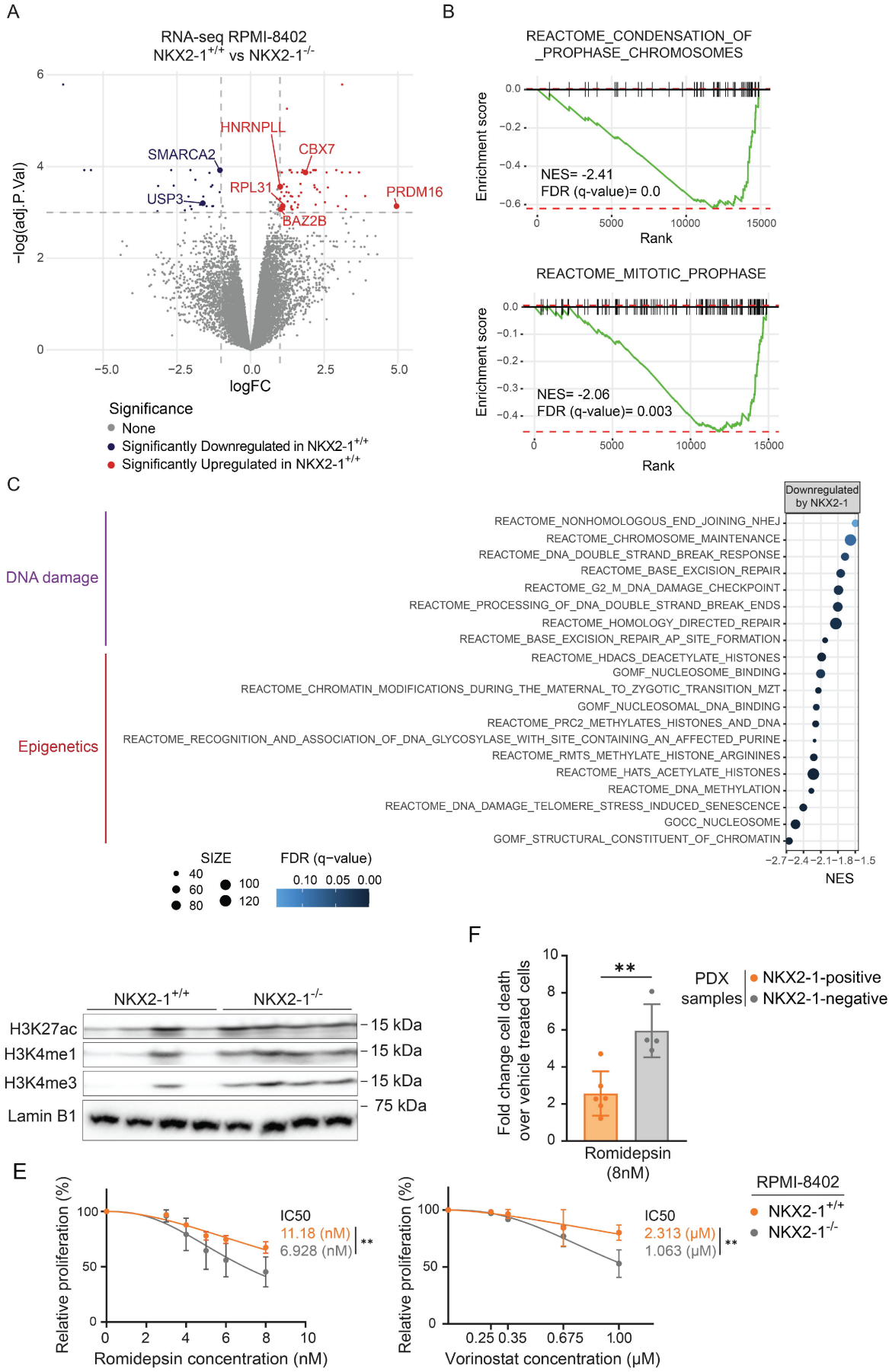
A
RNA-seq RPMI-8402
NKX2-1+/+ vs NKX2-1-/-
HNRNPLL
CBX7
SMARCA2
RPL31
PRDM16
USP3
BAZ2B
−log(adj.P.Val)
logFC
Significance
None
Significantly Downregulated in NKX2-1+/+
Significantly Upregulated in NKX2-1+/+
B
REACTOME_CONDENSATION_OF
_PROPHASE_CHROMOSOMES
Enrichment score
NES= -2.41
FDR (q-value)= 0.0
Rank
REACTOME_MITOTIC_PROPHASE
NES= -2.06
FDR (q-value)= 0.003
C
Downregulated by NKX2-1
DNA damage
Epigenetics
REACTOME_NONHOMOLOGOUS_END_JOINING_NHEJ
REACTOME_CHROMOSOME_MAINTENANCE
REACTOME_DNA_DOUBLE_STRAND_BREAK_RESPONSE
REACTOME_BASE_EXCISION_REPAIR
REACTOME_G2_M_DNA_DAMAGE_CHECKPOINT
REACTOME_PROCESSING_OF_DNA_DOUBLE_STRAND_BREAK_ENDS
REACTOME_HOMOLOGY_DIRECTED_REPAIR
REACTOME_BASE_EXCISION_REPAIR_AP_SITE_FORMATION
REACTOME_HDACS_DEACETYLATE_HISTONES
GOMF_NUCLEOSOME_BINDING
REACTOME_CHROMATIN_MODIFICATIONS_DURING_THE_MATERNAL_TO_ZYGOTIC_TRANSITION_MZT
GOMF_NUCLEOSOMAL_DNA_BINDING
REACTOME_PRC2_METHYLATES_HISTONES_AND_DNA
REACTOME_RECOGNITION_AND_ASSOCIATION_OF_DNA_GLYCOSYLASE_WITH_SITE_CONTAINING_AN_AFFECTED_PURINE
REACTOME_RMTS_METHYLATE_HISTONE_ARGININES
REACTOME_HATS_ACETYLATE_HISTONES
REACTOME_DNA_METHYLATION
REACTOME_DNA_DAMAGE_TELOMERE_STRESS_INDUCED_SENESCENCE
GOCC_NUCLEOSOME
GOMF_STRUCTURAL_CONSTITUENT_OF_CHROMATIN
NES
SIZE
FDR (q−value)
D
NKX2-1+/+
NKX2-1-/-
H3K27ac
H3K4me1
H3K4me3
Lamin B1
15 kDa
15 kDa
15 kDa
75 kDa
E
Relative proliferation (%)
IC50
11.18 (nM)
6.928 (nM)
Romidepsin concentration (nM)
IC50
2.313 (μM)
1.063 (μM)
Vorinostat concentration (μM)
RPMI-8402
NKX2-1+/+
NKX2-1-/-
F
Fold change cell death
over vehicle treated cells
Romidepsin
(8nM)
PDX
samples
NKX2-1-positive
NKX2-1-negative

Figure 4

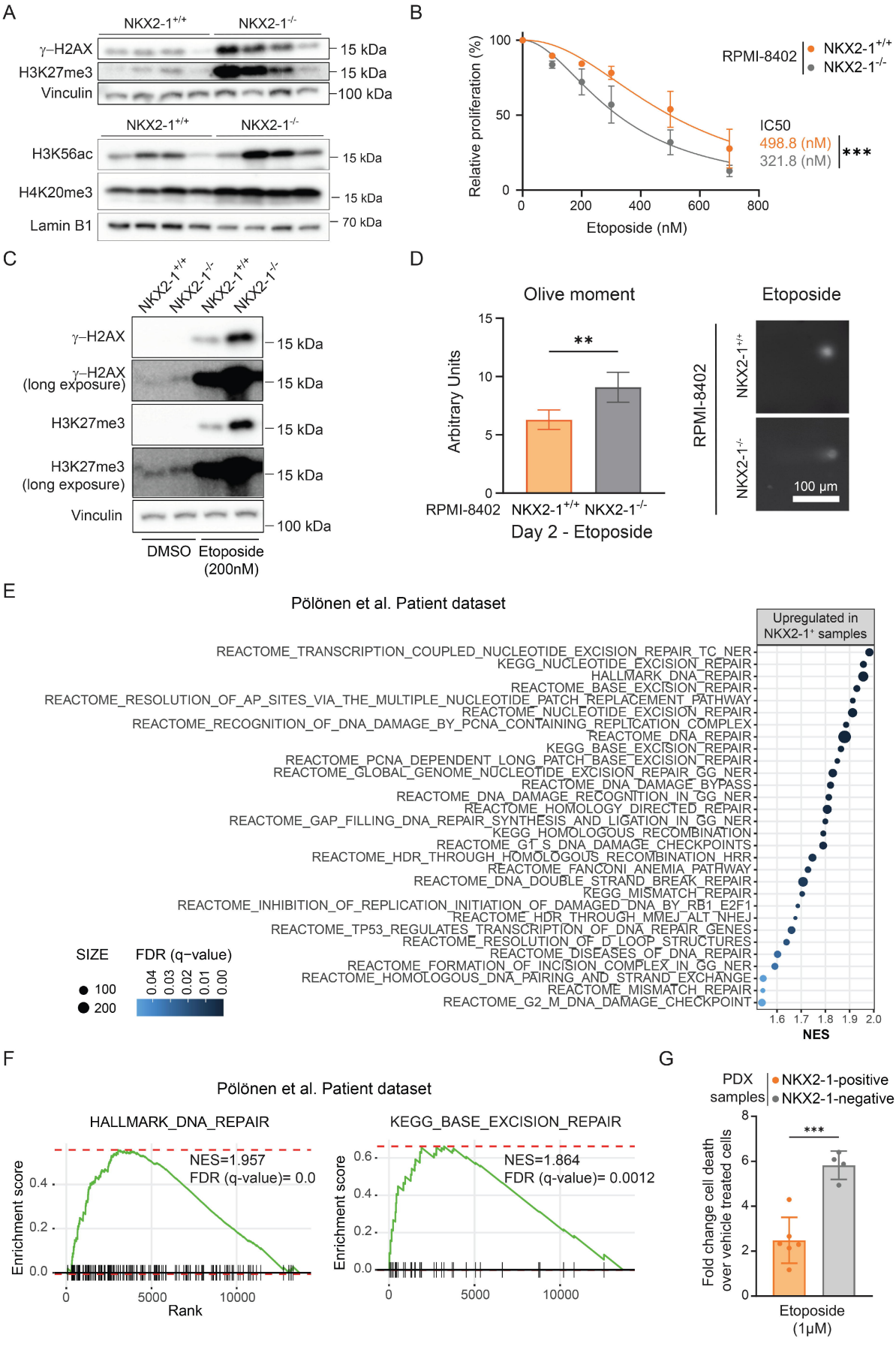
A
NKX2-1+/+
NKX2-1-/-
γ–H2AX
H3K27me3
Vinculin
15 kDa
15 kDa
100 kDa
H3K56ac
H4K20me3
Lamin B1
15 kDa
15 kDa
70 kDa
B
RPMI-8402
NKX2-1+/+
NKX2-1-/-
IC50
498.8 (nM)
321.8 (nM)
***
Relative proliferation (%)
Etoposide (nM)
C
γ–H2AX
γ–H2AX (long exposure)
H3K27me3
H3K27me3 (long exposure)
Vinculin
DMSO
Etoposide (200nM)
D
Olive moment
Etoposide
Arbitrary Units
**
RPMI-8402
Day 2 - Etoposide
100 μm
E
Pölönen et al. Patient dataset
Upregulated in NKX2-1+ samples
REACTOME_TRANSCRIPTION_COUPLED_NUCLEOTIDE_EXCISION_REPAIR_TC_NER
KEGG_NUCLEOTIDE_EXCISION_REPAIR
HALLMARK_DNA_REPAIR
REACTOME_BASE_EXCISION_REPAIR
REACTOME_RESOLUTION_OF_AP_SITES_VIA_THE_MULTIPLE_NUCLEOTIDE_PATCH_REPLACEMENT_PATHWAY
REACTOME_NUCLEOTIDE_EXCISION_REPAIR
REACTOME_RECOGNITION_OF_DNA_DAMAGE_BY_PCNA_CONTAINING_REPLICATION_COMPLEX
REACTOME_DNA_REPAIR
KEGG_BASE_EXCISION_REPAIR
REACTOME_PCNA_DEPENDENT_LONG_PATCH_BASE_EXCISION_REPAIR
REACTOME_GLOBAL_GENOME_NUCLEOTIDE_EXCISION_REPAIR_GG_NER
REACTOME_DNA_DAMAGE_BYPASS
REACTOME_DNA_DAMAGE_RECOGNITION_IN_GG_NER
REACTOME_HOMOLOGY_DIRECTED_REPAIR
REACTOME_GAP_FILLING_DNA_REPAIR_SYNTHESIS_AND_LIGATION_IN_GG_NER
KEGG_HOMOLOGOUS_RECOMBINATION
REACTOME_G1_S_DNA_DAMAGE_CHECKPOINTS
REACTOME_HDR_THROUGH_HOMOLOGOUS_RECOMBINATION_HRR
REACTOME_FANCONI_ANEMIA_PATHWAY
REACTOME_DNA_DOUBLE_STRAND_BREAK_REPAIR
KEGG_MISMATCH_REPAIR
REACTOME_INHIBITION_OF_REPLICATION_INITIATION_OF_DAMAGED_DNA_BY_RB1_E2F1
REACTOME_HDR_THROUGH_MMEJ_ALT_NHEJ
REACTOME_TP53_REGULATES_TRANSCRIPTION_OF_DNA_REPAIR_GENES
REACTOME_RESOLUTION_OF_D_LOOP_STRUCTURES
REACTOME_DISEASES_OF_DNA_REPAIR
REACTOME_FORMATION_OF_INCISION_COMPLEX_IN_GG_NER
REACTOME_HOMOLOGOUS_DNA_PAIRING_AND_STRAND_EXCHANGE
REACTOME_MISMATCH_REPAIR
REACTOME_G2_M_DNA_DAMAGE_CHECKPOINT
SIZE
FDR (q-value)
NES
F
Pölönen et al. Patient dataset
HALLMARK_DNA_REPAIR
NES=1.957
FDR (q-value)= 0.0
KEGG_BASE_EXCISION_REPAIR
NES=1.864
FDR (q-value)= 0.0012
Enrichment score
Rank
G
PDX samples
NKX2-1-positive
NKX2-1-negative
***
Fold change cell death over vehicle treated cells
Etoposide (1μM)

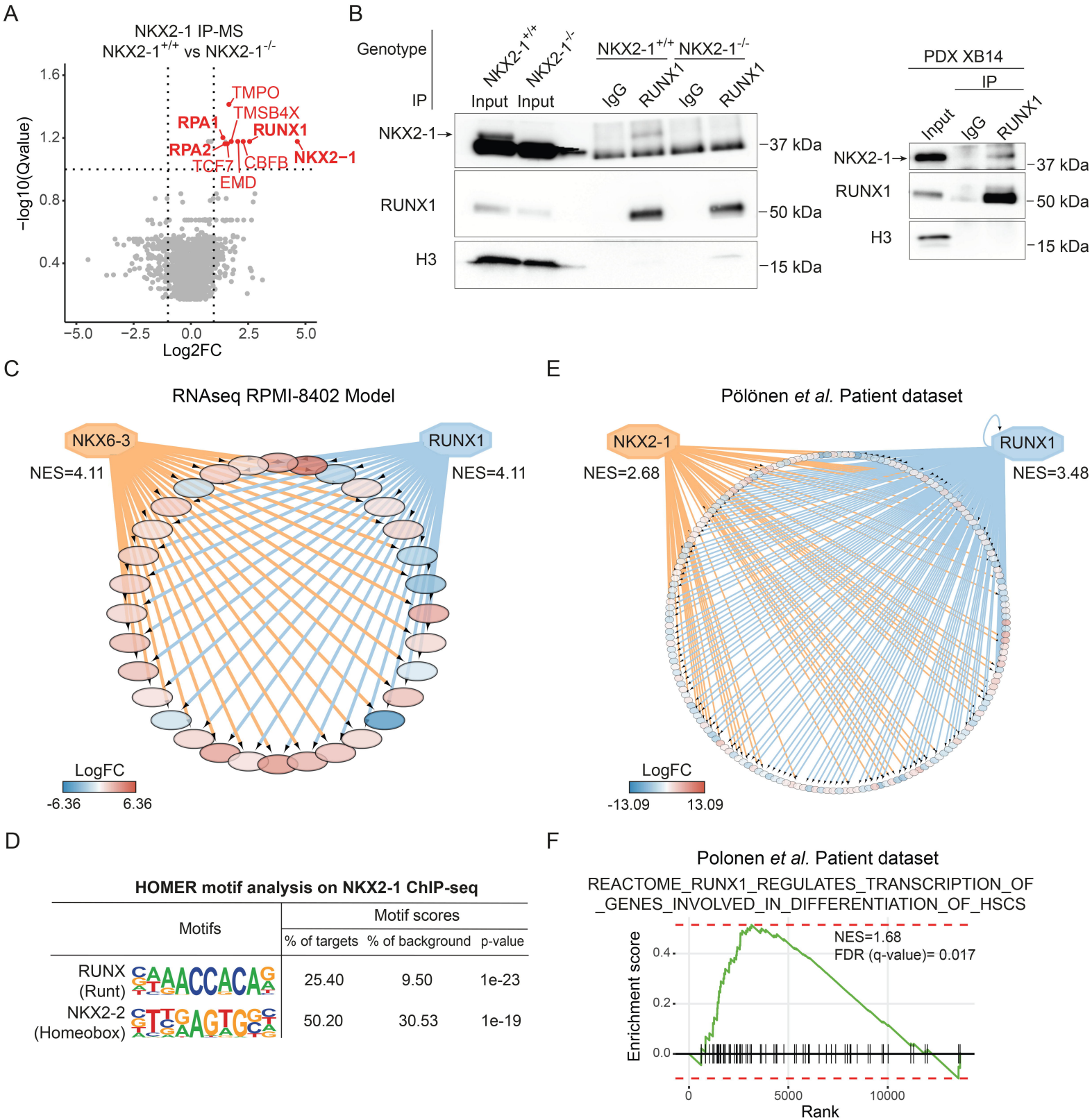
A
NKX2-1 IP-MS
NKX2-1+/+ vs NKX2-1-/-
−log10(Qvalue)
Log2FC
TMPO
TMSB4X
RPA1
RUNX1
RPA2
TCF7
CBFB
NKX2−1
EMD
B
Genotype
IP
Input Input
IgG
RUNX1
NKX2-1
RUNX1
H3
37 kDa
50 kDa
15 kDa
PDX XB14
C
RNAseq RPMI-8402 Model
NKX6-3
NES=4.11
RUNX1
NES=4.11
LogFC
-6.36
6.36
D
HOMER motif analysis on NKX2-1 ChIP-seq
Motifs
Motif scores
% of targets
% of background
p-value
RUNX (Runt)
25.40
9.50
1e-23
NKX2-2 (Homeobox)
50.20
30.53
1e-19
E
Pölönen et al. Patient dataset
NKX2-1
NES=2.68
RUNX1
NES=3.48
LogFC
-13.09
13.09
F
Polonen et al. Patient dataset
REACTOME_RUNX1_REGULATES_TRANSCRIPTION_OF_GENES_INVOLVED_IN_DIFFERENTIATION_OF_HSCS
NES=1.68
FDR (q-value)= 0.017
Enrichment score
Rank

Figure 6

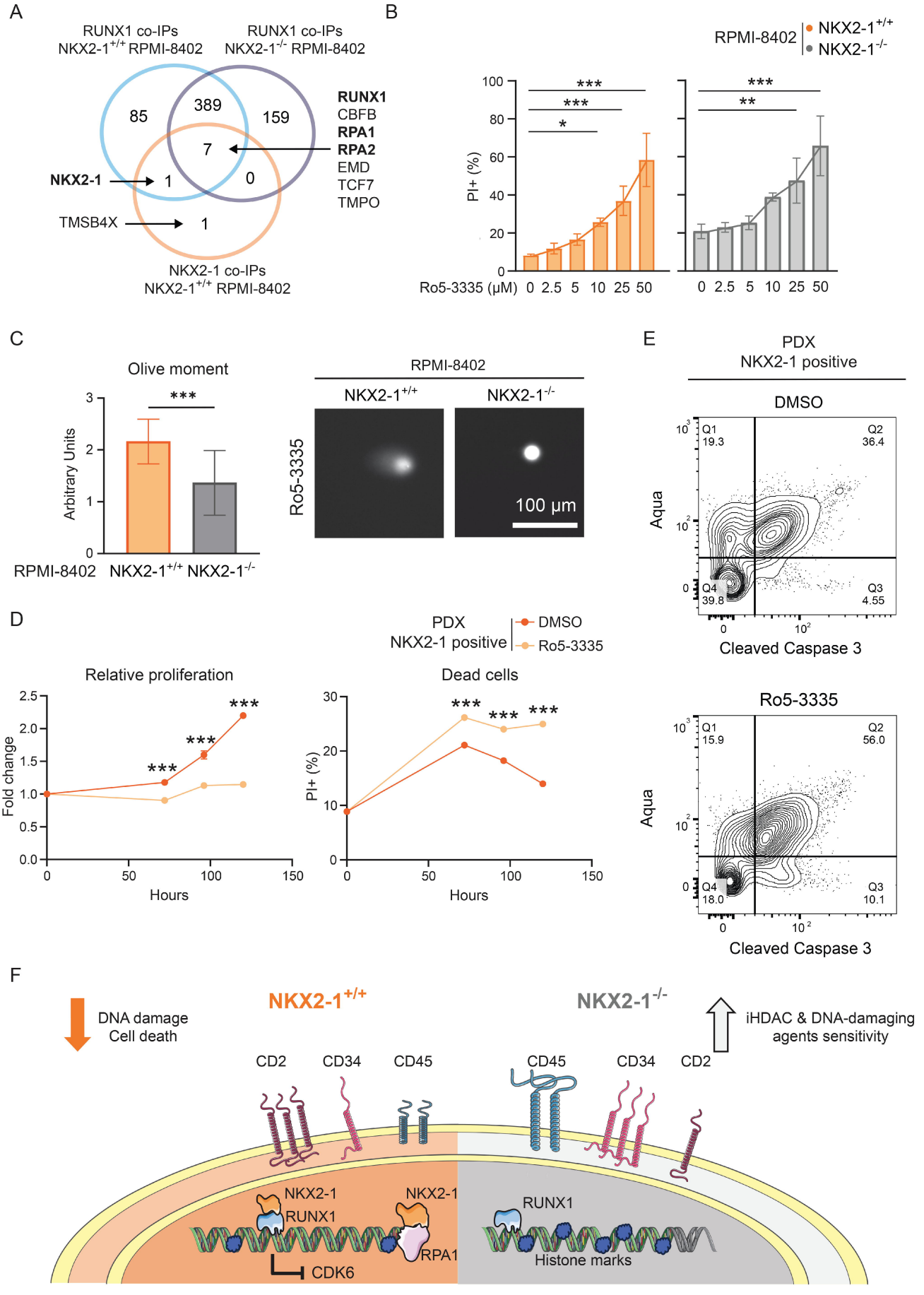
A
RUNX1 co-IPs NKX2-1+/+ RPMI-8402
RUNX1 co-IPs NKX2-1-/- RPMI-8402
85
389
159
7
NKX2-1
1
0
TMSB4X
1
NKX2-1 co-IPs NKX2-1+/+ RPMI-8402
RUNX1
CBFB
RPA1
RPA2
EMD
TCF7
TMPO
B
RPMI-8402
NKX2-1+/+
NKX2-1-/-
PI+ (%)
Ro5-3335 (μM) 0 2.5 5 10 25 50
C
Olive moment
Arbitrary Units
RPMI-8402 NKX2-1+/+ NKX2-1-/-
RPMI-8402
NKX2-1+/+
NKX2-1-/-
Ro5-3335
100 μm
D
PDX NKX2-1 positive
DMSO
Ro5-3335
Relative proliferation
Fold change
Hours
Dead cells
PI+ (%)
Hours
E
PDX NKX2-1 positive
DMSO
Aqua
Q1 19.3
Q2 36.4
Q4 39.8
Q3 4.55
Cleaved Caspase 3
Ro5-3335
Q1 15.9
Q2 56.0
Q4 18.0
Q3 10.1
Cleaved Caspase 3
F
DNA damage Cell death
NKX2-1+/+
NKX2-1-/-
iHDAC & DNA-damaging agents sensitivity
CD2
CD34
CD45
CD45
CD34
CD2
NKX2-1
RUNX1
NKX2-1
RPA1
CDK6
RUNX1
Histone marks

SUPPLEMENTARY DATA

NKX2-1 regulates cell survival, maturation, and DNA-damage responses as a cofactor of RUNX1 in T-cell acute lymphoblastic leukemia.

This file contains:

- **SUPPLEMENTARY METHODS**
- **SUPPLEMENTARY REFERENCES**
- **SUPPLEMENTARY TABLE S2**
- **SUPPLEMENTARY FIGURES S1-S21**

TABLE S1 is provided as a separate excel file.

Legend TABLE S1: Description of 496 peaks identified by MACS2 in NKX2-1 ChIP-seq analysis.

SUPPLEMENTARY METHODS

Cell culture

RPMI-8402 (ACC 290), DND-41 (ACC 525), SUP-T1 (ACC 140), HPB-ALL (ACC 483), ALL-SIL (ACC 511), LOUCY (ACC 394), PEER (ACC 6), PF-382 (ACC 38), MOLT-4 (ACC 362), MOLT-16 (ACC 29) and HEK-293T (ACC 635) cell lines were obtained from the German Collection of Microorganisms and Cell Cultures GmbH (DSMZ) and Jurkat (TIB-152) from ATCC. T-ALL cells were cultured in RPMI-1640 (Gibco) supplemented with 10% Fetal Calf Serum (FCS) (Gibco). HEK-293T cells were grown in DMEM (Thermo Fisher Scientific) supplemented with 10% fetal bovine serum (Thermo Fisher Scientific, #1017760). OP9-hDLL4 cells (kindly gifted by Tom Taghon) were grown in α-MEM medium (Invitrogen) supplemented with 20% FBS. All cells grew in a humidified cell-culture incubator at 37°C with 5% CO_2, except for OP9-hDLL4 which was grown at 7% CO_2, and were regularly confirmed to be mycoplasma negative.

T-ALL cell line RNA-sequencing data

RNA-seq data from T-ALL cell lines were previously described in Atak *et al*. [1]

Immunoblotting

Cells were lysed in cell lysis buffer (CST, #9803) supplemented with 5 mM Na_3VO_4 and cOmplete protease inhibitor (Roche) and denatured in 1X Laemmli sample buffer (Bio-Rad) containing β-mercaptoethanol (Sigma-Aldrich) at 96°C for 10 min. Proteins were separated on 4-15% Criterion Tris-Glycine eXtended gels (Bio-Rad) and transferred to PVDF membranes. For analyzing histone marks, 12% gels were used (Bio-Rad). After the membranes were incubated with primary and secondary antibodies (**Table 1**), proteins were visualized through chemiluminescence on an Azure C600 (Azure Biosystems). Quantification was performed using the LI-COR Image Studio Lite software using vinculin, histone 3 or Lamin B1 for protein input normalization.

Table 1. Primary and secondary antibodies used for immunoblotting

Target	Catalog number	Company	Target	Catalog number	Company
TTF1/NKX2-1	ab76013	Abcam	H3K27ac	ab4729	Abcam
RUNX1	PA5-19638	Thermo Fisher Scientific	H3K27me3	9733	Cell Signaling Technology
γ–H2AX	9718	Cell Signaling	H3K4me1	39297	Actif Motif

		Technology			
Histone 3	4620	Cell Signaling Technology	H3K4me3	ab8580	Abcam
H3K56ac	MA553741	Invitrogen	H4K20me3	703863	Invitrogen
RPA1	2267	Cell Signaling Technology	CD45	sc-25590	Santa Cruz
CDK6	3136	Cell Signaling Technology	Lamin B1	66095-1-Ig	Proteintech
Vinculin	V9131	Sigma	Tubulin	T5168	Sigma
2^{ndary} anti-Mouse	31432	Thermo Fisher Scientific	2^{ndary} anti-Rabbit	31462	Thermo Fisher Scientific
2^{ndary} anti-Rabbit light chain specific	SA00001-7L	Proteintech			

Quantitative RT-PCR

Total RNA was extracted with RNeasy kit (Qiagen) followed by cDNA synthesis of 500 ng RNA using GoScript reverse transcriptase with random primers (Promega). mRNA expression levels of *NKX2-1* (Fw-AACCAAGCGCATCCAATCTCAAGG; Rv-TGTGCCCAGAGTGAAGTTTGGTCT) and *CDK6* (Fw-TCCCTCCTTTGAAGTGGATG; Rv-GTCACCTGGGGCTAAATGAA) together with *ACTB* (Fw-GTCACCAACTGGGACGACAT; Rv-GAGGCGTACAGGGATAGCAC) as a reference gene were analyzed in triplicates with SYBR Green qRT-PCR (Promega) on a CFX Connect Instrument (BioRad) and quantified using the $\Delta\Delta$Ct method.

Flow cytometry

Immunophenotyping was performed using the antibodies listed in **Table 2**. Proliferation was assessed by cell cycle analysis. Cells were fixed and permeabilized with 70% ethanol, followed by a stain of the DNA by using propidium iodide (PI) with RNAse A. Apoptosis was evaluated by analyzing annexin-V PE (BioLegend, #640947) in binding buffer (10 mM HEPES, 140 mM NaCl, 2.5 mM $CaCl_2$ at pH 7.4) or cleaved caspase 3 (Cell Signaling Technology, #9664) followed by a secondary staining with an Alexa Fluor 488 conjugated anti-rabbit antibody (Thermo Fisher Scientific, #A-11070) in cells fixed and permeabilized with 70% ethanol. Zombie Aqua staining (BioLegend, #423102) was used as a cell viability marker. For viability and drug sensitivity assays, viable cells counts were defined as the proportion of single cells not staining for PI and cell death as single cells staining for PI. For specific cell death, an adaptation of the formula previously described[2] was used: [(% PI positive in the assay well) – (% PI positive in the control well) × 100] ÷ [100 – (% PI positive in the control well)]. O-propargyl puromycin (OPP) labeling was performed according to manufacturer's instructions using the Click-IT OPP Alexa Fluor 647 Protein synthesis Assay kit (Thermo Fisher Scientific, #C10458). Samples were measured on a MACSQuant X flow cytometer (Miltenyi). All data were analyzed using FlowJo software (v10.9).

Table 2. Conjugated antibodies used for immunophenotyping.

Target	Catalog number	Company	Target	Catalog number	Company
CD1a	A07742	Beckman Coulter	CD5	345783	BD Bioscience
CD2	335786	BD Bioscience	CD7	347483	BD Bioscience
sCD3	341101	BD Bioscience	CD34	348053	BD Bioscience
cyCD3	345767	BD Bioscience			

ChIP-sequencing and analysis

For NKX2-1 ChIP-seq: 30 million RPMI-8402 cells were cross-linked for 10 min in 1% formaldehyde, followed by quenching with 0.125M glycine and two washes in ice-cold PBS. Cells were subsequently

sonicated on a Bioruptor NGS (Diagenode) for 12 cycles of 30 s activity – 30 s rest. ChIP was performed using the SimpleChIP Plus Sonication Chromatin IP kit (Cell Signaling), Dynabeads Protein G (Invitrogen) magnetic beads and anti-TTF1/NKX2-1 antibody (Abcam, #ab76013) according to the manufacturer's instructions. DNA was purified using PCR purification columns (Qiagen). KAPA HyperPlus library was constructed and sequenced on the Illumina HiSeq 4000 platform. Obtained single-end 50 bp reads were mapped to the NCBI human reference genome (GRCh38) using Bowtie2 (v2.4.4), filtered using SAMtools (MACQS > 30, v1.18) and deduplicated with Picard (v2.18.23). Next, peaks were called with MACS2 using the NKX2-1$^{-/-}$ clones as background samples and a p-value cut-off of 0.01. Motif analysis was performed using HOMER (v4.11) with default settings.[3] Finally, the peaks were annotated using ChIPseeker (v1.30.3),[4,5] considering the region 3000 bp up- and downstream of the transcription start site (TSS) as the promoter region.

For H3K27ac ChIP-seq: 30 million RPMI-8402 cells were cross-linked for 10 min in 1% formaldehyde, followed by quenching with 0.125M glycine and two washes in ice-cold PBS. For nuclei isolation, cells were resuspended in 1X RSB buffer (10 mM Tris at pH7.4, 10 mM NaCl, 3 mM $MgCl_2$) and left on ice for 10 min to swell. Cells were collected by centrifugation and resuspended in RSBG40 buffer (10 mM Tris at pH7.4, 10 mM NaCl, 3 mM $MgCl_2$, 10% glycerol, 0.5% NP-40) with 1/10 v/v of 10% detergent (3.3% w/v sodium deoxycholate, 6.6% v/v Tween-40). Nuclei were collected by centrifugation and resuspended in L3B+ buffer (10 mM Tris-Cl at pH 8.0, 100 mM NaCl, 1 mM EDTA, 0.5 mM EGTA, 0.1% Na-Deoxycholate, 0.5% N-Lauroylsarcosine, 0.2% SDS). Samples were subsequently sonicated on a Bioruptor NGS (Diagenode) for 10 cycles of 30 s activity – 30 s rest. The chromatin was supplemented with 1% Triton-X100 after fragmentation. H3K27ac antibody (Abcam, #ab4729) was preconjugated to magnetic protein-G beads (Cell Signaling Technology). Chromatin immunoprecipitation was carried out overnight. Tagmentation and library preparation were performed using the Nextera DNA library prep kit (Illumina). DNA was purified using triple sided SPRI bead clean-up (1.2X, 0.6X, 0.9X). (Agencourt AMPure Beads, Beckman Coulter). Sequencing was carried out on an Illumina HiSeq 4000 platform. The raw ChIPmentation sequencing data were first cleaned with fastq-MCF (ea-utils) followed by quality control with fastQC. Reads were mapped to the NCBI human reference genome (GRCh38) using Bowtie2 (v2.4.4), filtered using SAMtools (MACQS > 30, v1.18) and deduplicated with Picard (v2.18.23). Peaks were called with the MACS2 software (v2.2.9.1) and the signals were normalised using DeepTools (v3.5.6).

ATAC sequencing data in RPMI-8402 cells and RUNX1 ChIP-seq in various cell lines data were obtained from the web tool by Oki, S; Ohta, T (2015): ChIP-Atlas. https://chip-atlas.org. [6–8]

Luciferase reporter assays

HEK-293T cells were transfected with a dual-luciferase reporter plasmid containing the identified CDK6 enhancer region chr7:92754552-92755863 (hg38) (**Figure S5A**, VectorBuilder ID: VB250521-1459nsy) as well as with an NKX2-1[9] and/or RUNX1 (Origene code: rc223809) overexpression or control plasmid (pMSCV-GFP) in a 6-well plate using Lipofectamine 3000 (Thermo Fisher Scientific, #L3000001). After 48 h, the cells were lysed, and Firefly and Renilla luciferase expression was measured consecutively using the Dual-Luciferase Reporter Assay System (Promega, E1910) on a Victor X4 multilabel microplate reader (PerkinElmer). Background signal was subtracted from luciferase signals before calculating the relative Firefly/Renilla ratio and normalizing to the control reporter.

Polysome profiling

A 15-55% continuous sucrose gradient was prepared by sequentially layering sucrose solutions of 55%, 45%, 35%, 25%, and 15% containing 20mM HEPES at pH 7.4, 100mM KCl, 10mM $MgCl_2$,

0.1mg/mL Cycloheximide (CHX). Tubes were frozen at -80°C after each layer addition. 20 million cells were treated for 5min with 0.1 µg/µL CHX prior to lysis with lysis buffer containing 5 mM Tris-HCl at pH 7.4, 1.5 mM KCl, 2.5 mM $MgCl_2$, 2 mM Dithiothreitol (DTT), 0.5% Sodium Deoxycholate, 0.5% Triton-X100, 0.1 µg/µL CHX and cOmplete protease inhibitor (Roche). Lysates were cleared by centrifugation (20,000 g, 5 min, 4°C) and gently loaded on top of the thawed sucrose gradients that were subsequently ultracentrifuged (37,000 rpm, 2.5 h, 4°C). Afterwards, the gradients were analyzed for 254 nm absorbance on a BioLogic LP system (BioRad). The polysome profile data was processed and visualized using RStudio (R v4.1.0).

Compounds

Compounds used were Romidepsin (Cayman Chemical), Vorinostat (Cayman Chemical), Etoposide (Selleckchem), Doxorubicin (Cayman Chemical), 6-TG (Tebubio N.V.), Ro5-3335 (MedChemExpress) and AI-10-47 (MedChemExpress). All compounds were dissolved in DMSO.

Alkaline Comet Assay

After drug treatment as specified in the figure legends, cells were mixed with 0.4% low-melting-temperature agarose before being loaded onto slides coated with 1.5% normal agarose. These slides were then lysed overnight at 4°C in a lysis buffer containing 2.5 M NaCl, 10 mM Tris at pH 10.0, 100 mM EDTA, 1% Triton X-100, 1% N-lauroylsarcosine. The slides were further immersed for 20 min in cold electrophoresis buffer containing 0.3 M NaOH, 1 mM EDTA at pH 13.0, followed by electrophoresis (30 mins at 1 V/cm). The slides were then stained with propidium iodide (2.5 µg/mL), visualized under a Nikon Ti2 spinning-disk confocal fluorescence microscope (Tokyo, Japan), and analyzed by OpenComet in Imagej v1.3.1.[10]

Mass spectrometry

Immunoprecipitated samples were eluted, pre-processed and subjected to LC-mass spectrometry at the KU Leuven Proteomics core facility. All spectra were compared against the Human reference proteome database (https://www.uniprot.org/proteomes/UP000005640) using default Spectronaut (v19.2.240905.62635) settings with background level imputation. To identify NKX2-1 binding partners, NKX2-1 co-immunoprecipitated proteins with a fold change above 2 detected in NKX2-$1^{+/+}$ samples against NKX2-$1^{-/-}$ samples, with a q-value below 0.1 and an abundance higher than measured in the IgG-control sample were retained. To analyze the RUNX1 co-immunoprecipitated proteins, only proteins with a fold change above 1.5 and a q-value below 0.05 in the comparison of NKX2-$1^{+/+}$ against NKX2-$1^{-/-}$ samples were retained, with the additional requirement that retained proteins also had to show a fold change above 2 and a q-value below 0.05 compared to the respective IgG samples of their matching genotype. Results were visualized using RStudio (R v4.1.0). The mass spectrometry proteomics data have been deposited to the ProteomeXchange Consortium via the PRIDE partner repository with dataset identifiers PXD057622 and PXD057654.[11]

Patient-derived xenograft (PDX) /OP9-hDLL4 cocultures

2-3 million T-ALL PDX-XB14 cells were seeded onto 6-well plates containing a confluent layer of OP9-hDLL4 cells.[12] After 6 days of PDX/OP9 coculture in α-MEM medium supplemented with 20% FBS, 100 µg/mL Primocin (Invivogen) and 20 ng/mL IL-7 Human Recombinant (200-07, Peprotech) and grown at 7% CO_2, cells were collected for immunoprecipitation or western blotting. For drug treatment experiments, 0.3 million T-ALL PDX cells of each analyzed PDX sample were seeded onto 48-well plates previously seeded with OP9-hDLL4 cells, except for the case of Ro5-3335 where no OP9-hDLL4 were used, in α-MEM medium supplemented with 20% FBS, 100 µg/mL Primocin and 20 ng/mL IL-7 Human Recombinant grown at 7% CO_2.

Statistics

Statistical analyses were performed in GraphPad Prism 10 using the statistical tests indicated in the figure legends. T-tests were two-tailed unpaired. All data presented in the graphs have been checked for normality using the Shapiro-Wilk test. When the data met the assumptions of normality, subsequent analyses were conducted using parametric tests (unpaired t-test). If the data did not meet normality criteria, non-parametric alternatives were applied (Mann–Whitney test). When appropriate, one-way or two-way ANOVA was performed followed by a Tukey's HSD post hoc test or Šidák test. When the data were not normally distributed, a Kruskal-Wallis test followed by a Dunn's post hoc test was applied. The figure legends specify the statistical test used in each figure panel.

SUPPLEMENTARY REFERENCES

1. Kalender Atak Z, Gianfelici V, Hulselmans G, et al. Comprehensive Analysis of Transcriptome Variation Uncovers Known and Novel Driver Events in T-Cell Acute Lymphoblastic Leukemia. PLoS Genet 2013;9(12):e1003997.
2. Epling-Burnette PK, Liu JH, Catlett-Falcone R, et al. Inhibition of STAT3 signaling leads to apoptosis of leukemic large granular lymphocytes and decreased Mcl-1 expression. Journal of Clinical Investigation 2001;107(3):351–362.
3. Heinz S, Benner C, Spann N, et al. Simple Combinations of Lineage-Determining Transcription Factors Prime cis-Regulatory Elements Required for Macrophage and B Cell Identities. Mol Cell 2010;38(4):576–589.
4. Wang Q, Li M, Wu T, et al. Exploring Epigenomic Datasets by ChIPseeker. Curr Protoc 2022;2(10):e585.
5. Yu G, Wang LG, He QY. ChIP seeker: An R/Bioconductor package for ChIP peak annotation, comparison and visualization. Bioinformatics 2015;31(14):2382–2383.
6. Zou Z, Ohta T, Oki S. ChIP-Atlas 3.0: a data-mining suite to explore chromosome architecture together with large-scale regulome data. Nucleic Acids Res 2024;52(W1):W45–W53.
7. Zou Z, Ohta T, Miura F, Oki S. ChIP-Atlas 2021 update: a data-mining suite for exploring epigenomic landscapes by fully integrating ChIP-seq, ATAC-seq and Bisulfite-seq data. Nucleic Acids Res 2022;50(W1):W175–W182.
8. Oki S, Ohta T, Shioi G, et al. ChIP-Atlas: a data-mining suite powered by full integration of public ChIP-seq data. EMBO Rep 2018;19(12):e46255.
9. Heylen E, Verstraete P, Van Aerschot L, et al. Transcription factor NKX2-1 drives serine and glycine synthesis addiction in cancer. Br J Cancer 2023;128(10):1862–1878.
10. Gyori BM, Venkatachalam G, Thiagarajan PS, Hsu D, Clement M-V. OpenComet: An automated tool for comet assay image analysis. Redox Biol 2014;2457–465.
11. Perez-Riverol Y, Bai J, Bandla C, et al. The PRIDE database resources in 2022: A hub for mass spectrometry-based proteomics evidences. Nucleic Acids Res 2022;50(D1):D543–D552.
12. Van De Walle I, De Smet G, Gärtner M, et al. Jagged2 acts as a Delta-like Notch ligand during early hematopoietic cell fate decisions. Blood 2011;117(17):4449–4459.
13. Pölönen P, Di Giacomo D, Seffernick AE, et al. The genomic basis of childhood T-lineage acute lymphoblastic leukaemia. Nature 2024;632(8027):1082–1091.

SUPPLEMENTARY TABLES

TABLE S1 (Description of 496 peaks identified by MACS2 in NKX2-1 ChIP-seq analysis) is provided as a separate excel file.

TABLE S2. Top 25 known motifs identified by HOMER motif analysis ranked on p-value.

HOMER motif analysis on NKX2-1 ChIP-seq from NKX2-1 RPMI-8402 model

RANK	Motif	Name	% of targets	% of background	p-value
1		Fli1(ETS)/CD8-FLI-ChIP-Seq(GSE20898)/Homer	34.27%	15.09%	1e-25
2		RUNX2(Runt)/PCa-RUNX2-ChIP-Seq(GSE33889)/Homer	29.23%	11.90%	1e-24
3		RUNX(Runt)/HPC7-Runx1-ChIP-Seq(GSE22178)/Homer	25.40%	9.50%	1e-23
4		Etv2(ETS)/ES-ER71-ChIP-Seq(GSE59402)/Homer	30.65%	13.27%	1e-23
5		RUNX-AML(Runt)/CD4+-PolII-ChIP-Seq(Barski_et_al.)/Homer	25.60%	10.00%	1e-22
6		RUNX1(Runt)/Jurkat-RUNX1-ChIP-Seq(GSE29180)/Homer	31.85%	14.46%	1e-22
7		Elk4(ETS)/Hela-Elk4-ChIP-Seq(GSE31477)/Homer	19.76%	6.70%	1e-21
8		Elk1(ETS)/Hela-Elk1-ChIP-Seq(GSE31477)/Homer	19.35%	6.60%	1e-20
9		Nkx2.2(Homeobox)/NPC-Nkx2.2-ChIP-Seq(GSE61673)/Homer	50.20%	30.53%	1e-19
10		ELF1(ETS)/Jurkat-ELF1-ChIP-Seq(SRA014231)/Homer	17.94%	6.14%	1e-18
11		Nkx2.5(Homeobox)/HL1-Nkx2.5.biotin-ChIP-Seq(GSE21529)/Homer	52.02%	32.97%	1e-17
12		EWS:ERG-fusion(ETS)/CADO_ES1-EWS:ERG-ChIP-Seq(SRA014231)/Homer	25.60%	11.45%	1e-17
13		GABPA(ETS)/Jurkat-GABPa-ChIP-Seq(GSE17954)/Homer	25.60%	11.62%	1e-17
14		ETS(ETS)/Promoter/Homer	13.10%	3.82%	1e-16
15		ETV1(ETS)/GIST48-ETV1-ChIP-Seq(GSE22441)/Homer	34.27%	18.24%	1e-16
16		ETV4(ETS)/HepG2-ETV4-ChIP-Seq(ENCODE)/Homer	28.83%	14.13%	1e-16
17		STAT5(Stat)/mCD4+-Stat5-ChIP-Seq(GSE12346)/Homer	15.12%	5.18%	1e-15
18		EWS:FLI1-fusion(ETS)/SK_N_MC-EWS:FLI1-ChIP-Seq(SRA014231)/Homer	19.35%	7.81%	1e-15
19		ETS1(ETS)/Jurkat-ETS1-ChIP-Seq(GSE17954)/Homer	28.43%	14.21%	1e-15

20		ETS:RUNX(ETS,Runt)/Jurkat-RUNX1-ChIP-Seq(GSE17954)/Homer	6.45%	1.16%	1e-13
21		ERG(ETS)/VCaP-ERG-ChIP-Seq(GSE14097)/Homer	37.50%	22.36%	1e-13
22		Bapx1(Homeobox)/VertebralCol-Bapx1-ChIP-Seq(GSE36672)/Homer	51.21%	34.59%	1e-13
23		Nkx2.1(Homeobox)/LungAC-Nkx2.1-ChIP-Seq(GSE43252)/Homer	56.45%	40.72%	1e-11
24		Ets1-distal(ETS)/CD4+-PolII-ChIP-Seq(Barski_et_al.)/Homer	11.29%	3.86%	1e-11
25		ZNF189(Zf)/HEK293-ZNF189.GFP-ChIP-Seq(GSE58341)/Homer	23.19%	12.11%	1e-11

SUPPLEMENTARY FIGURES

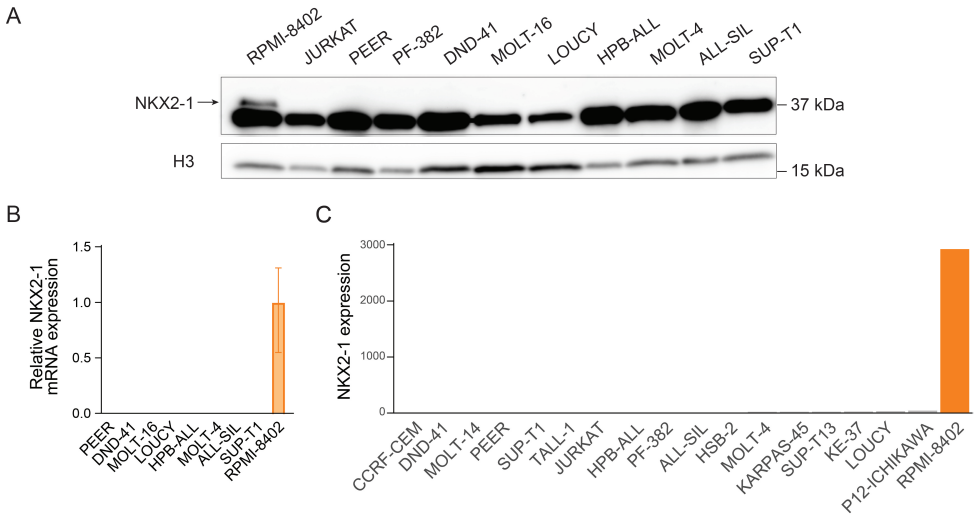

Figure S1. The RPMI-8402 cell line is the only analyzed human T-ALL cell line with endogenous NKX2-1 expression (A) Immunoblot for NKX2-1 in a panel of human T-ALL cell lines. The signal detected at 37 kDa in all cell lines corresponds to a nonspecific band detected by the NKX2-1 antibody. The NKX2-1 specific signal is indicated with an arrow. Histone 3 (H3) detection served as loading control. **(B)** Relative NKX2-1 mRNA expression in RPMI-8402 and other human T-ALL cell lines by RT-qPCR. **(C)** NKX2-1 mRNA expression in RPMI-8402 and 17 other human T-ALL cell lines from Atak *et al*. [1]

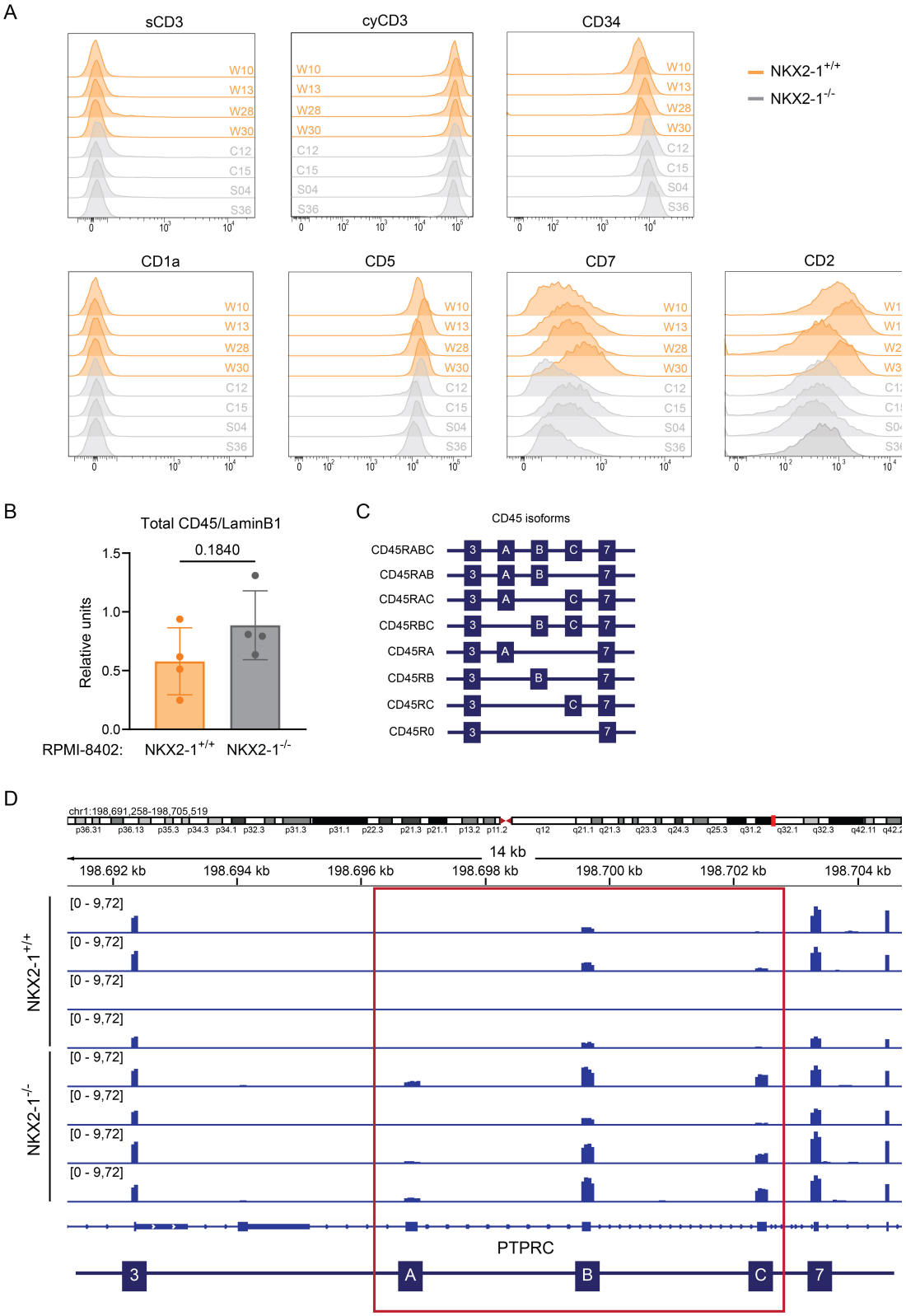

Figure S2. Immunophenotyping and CD45 isoform expression in NKX2-1$^{+/+}$ and NKX2-1$^{-/-}$ RPMI-8402 clones. **(A)** Histograms show flow cytometry signal per clone for each indicated marker. **(B)** Quantification of total CD45 protein expression by western blotting in NKX2-1$^{+/+}$ and NKX2-1$^{-/-}$ RPMI-8402 clones. Data are represented as mean ± SD. Individual dots represent 4 biologically independent clones per genotype. p-values were calculated using an unpaired two-tailed t-test. Western blot is shown in Figure 1D. **(C)** Scheme of PTPRC (CD45) exon-intron structure of the alternatively spliced region in PTPRC. **(D)** Normalized RNA-seq reads at the *PTPRC* locus in RPMI-8402 NKX2-1$^{+/+}$ and NKX2-1$^{-/-}$ clones in IGV. Exons A, B and C of *PTPRC* that exhibit differential splicing are shown at the bottom.

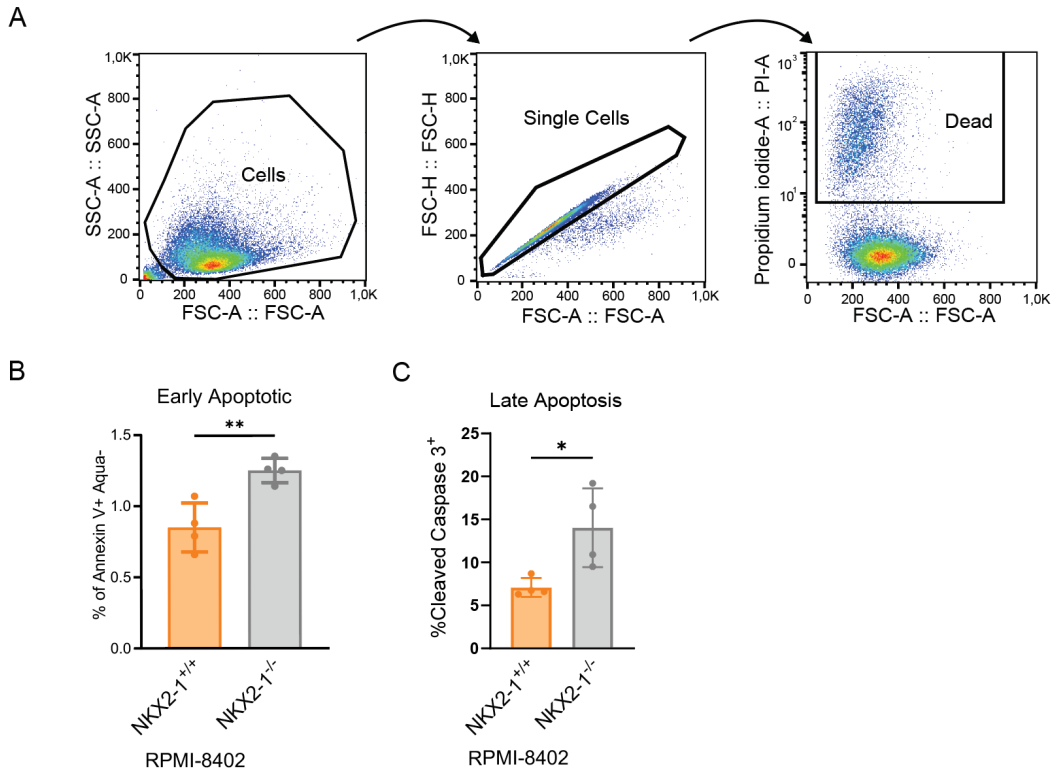

Figure S3. NKX2-1 decreases apoptosis in RPMI-8402 model. (A) Gating strategy for cell death using Propidium Iodide (PI) by flow cytometry. **(B)** Flow cytometry based quantification of Annexin V-positive/Zombie Aqua-negative early apoptotic cells in NKX2-1 $^{+/+}$ and NKX2-1$^{-/-}$ RPMI-8402 clones at day 5. Data represented as mean ± SD, statistics calculated by unpaired two-tailed t-test. **(C)** Flow cytometry based quantification of cleaved caspase 3-positive late apoptotic cells in NKX2-1 $^{+/+}$ and NKX2-1$^{-/-}$ RPMI-8402 clones at day 5. Data are represented as mean ± SD. Individual dots represent 4 biologically independent clones per genotype. p-values were calculated using an unpaired two-tailed t-test. *p-value < 0.05; **p-value < 0.01.

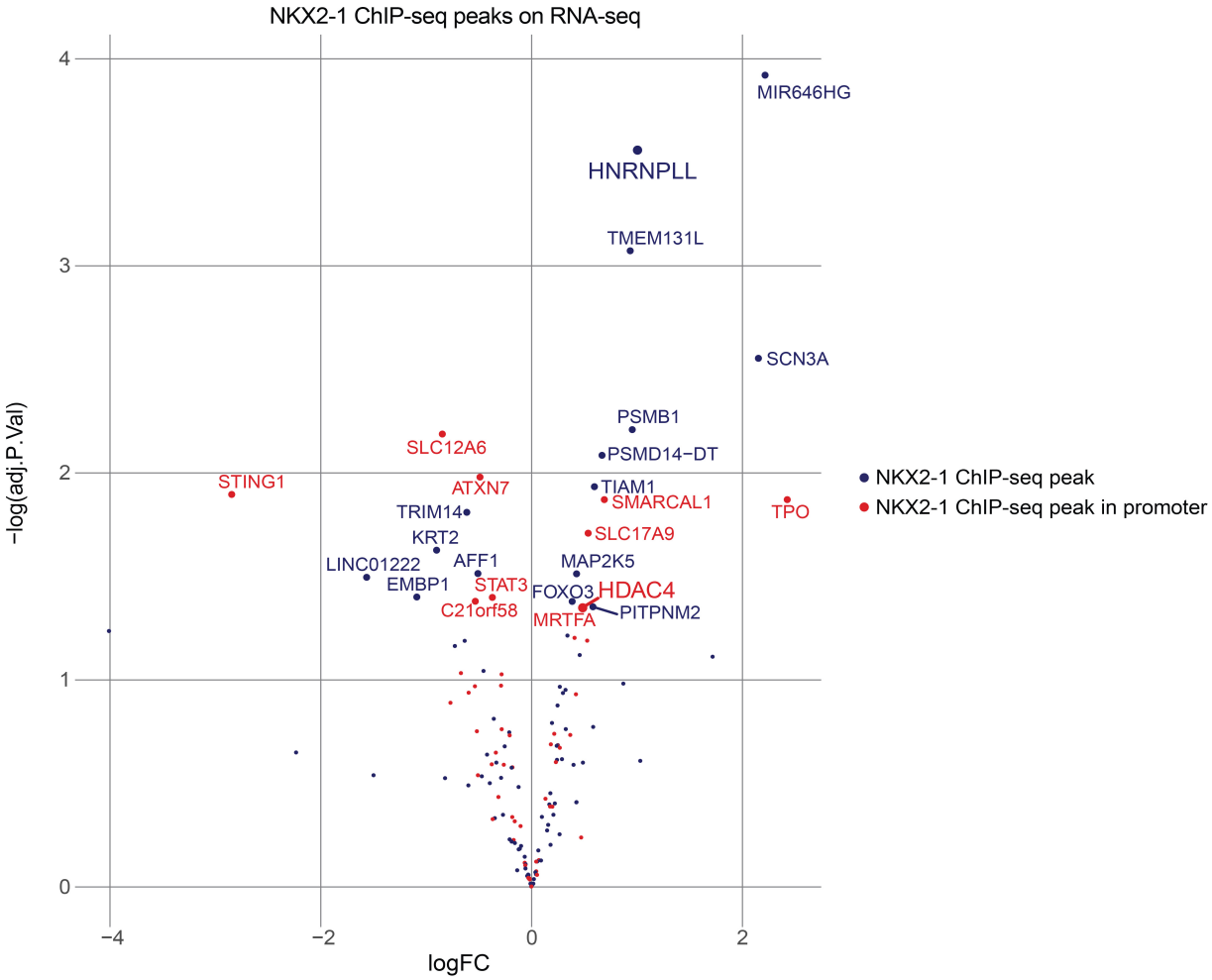

Figure S4. Overlap of RNA-seq and ChIP-seq data obtained from NKX2-1 RPMI-8402 model. Volcano plot showing RNA-seq based expression of genes in NKX2-1$^{+/+}$ versus NKX2-1$^{-/-}$ RPMI-8402 clones that have adjacent peaks in the NKX2-1 ChIP-seq experiment on RPMI-8402 cells. Genes with a significant RNA-seq expression change (–log(adj.P.Val) > 1.3) are labelled with their gene name. Red dots refer to genes with ChIP-seq signal in their promoter region, blue dots are genes with exonic, intronic, 3'UTR or distal intergenic ChIP-seq signal.

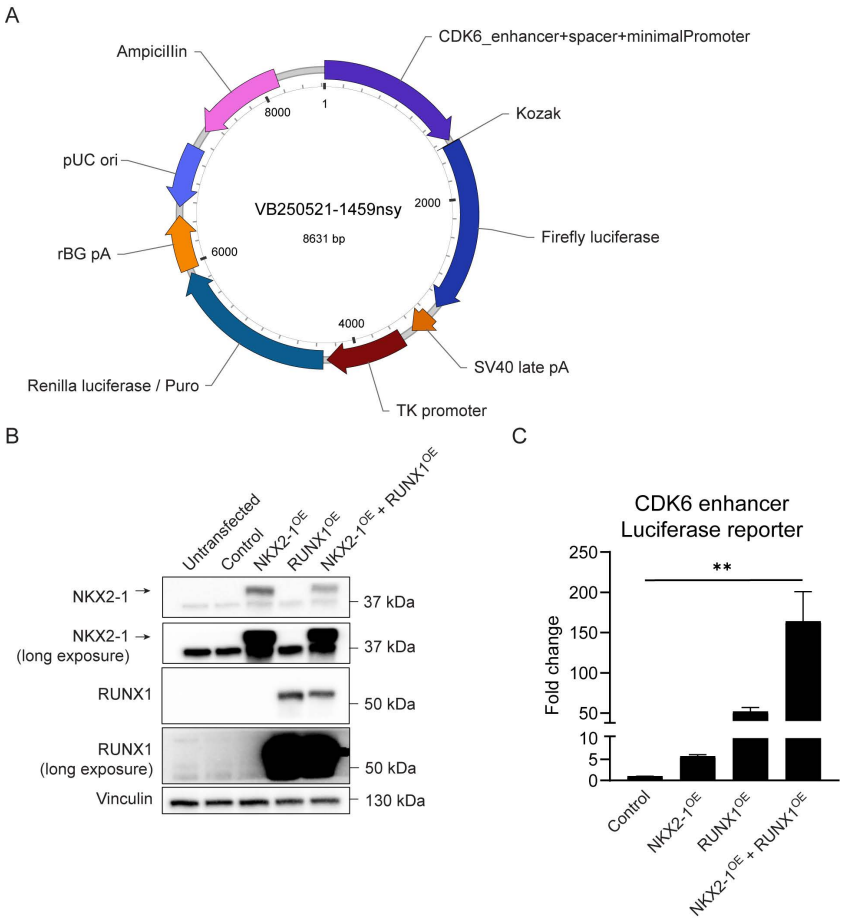

Figure S5. NKX2-1 and RUNX1 synergistically regulate CDK6 enhancer activity. (A) Dual-luciferase plasmid containing the CDK6 enhancer region. **(B)** Western blot analysis of NKX2-1 and RUNX1 expression in HEK-293T cells transfected with CDK6 enhancer luciferase plasmid and co-transfected with empty vector control (pMSCV-GFP), NKX2-1-overpression and/or RUNX1-overexpression plasmids. The NKX2-1 specific signal is indicated with an arrow. Vinculin detection served as loading control. **(C)** Results from dual-luciferase reporter assays in HEK-293T cells. The ratio of Firefly luciferase signal (controlled by CDK6 enhancer followed by minimal promoter) over Renilla luciferase signal (under constitutive TK promoter) serves as a measurement of CDK6 enhancer activity. The graph shows combined data from two independent experiments. Error bars indicate SD. Statistics calculated by Kruskal-Wallis followed by a Dunn's post hoc test: **p-value < 0.01

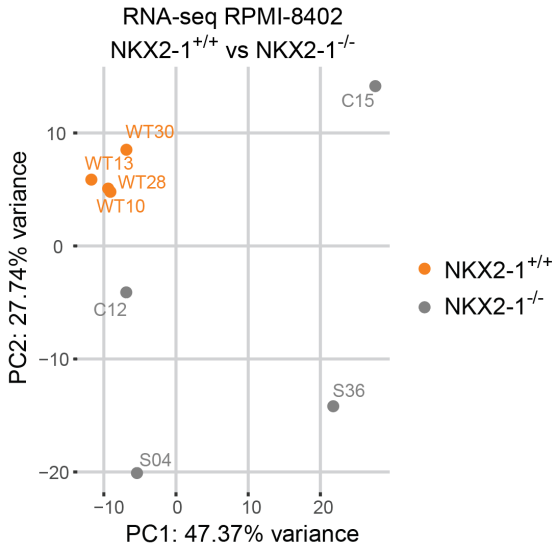

Figure S6. PCA plot showing the variation among the RNA-sequencing samples based on normalized expression data from NKX2-1$^{+/+}$ and NKX2-1$^{-/-}$ RPMI-8402 clones.

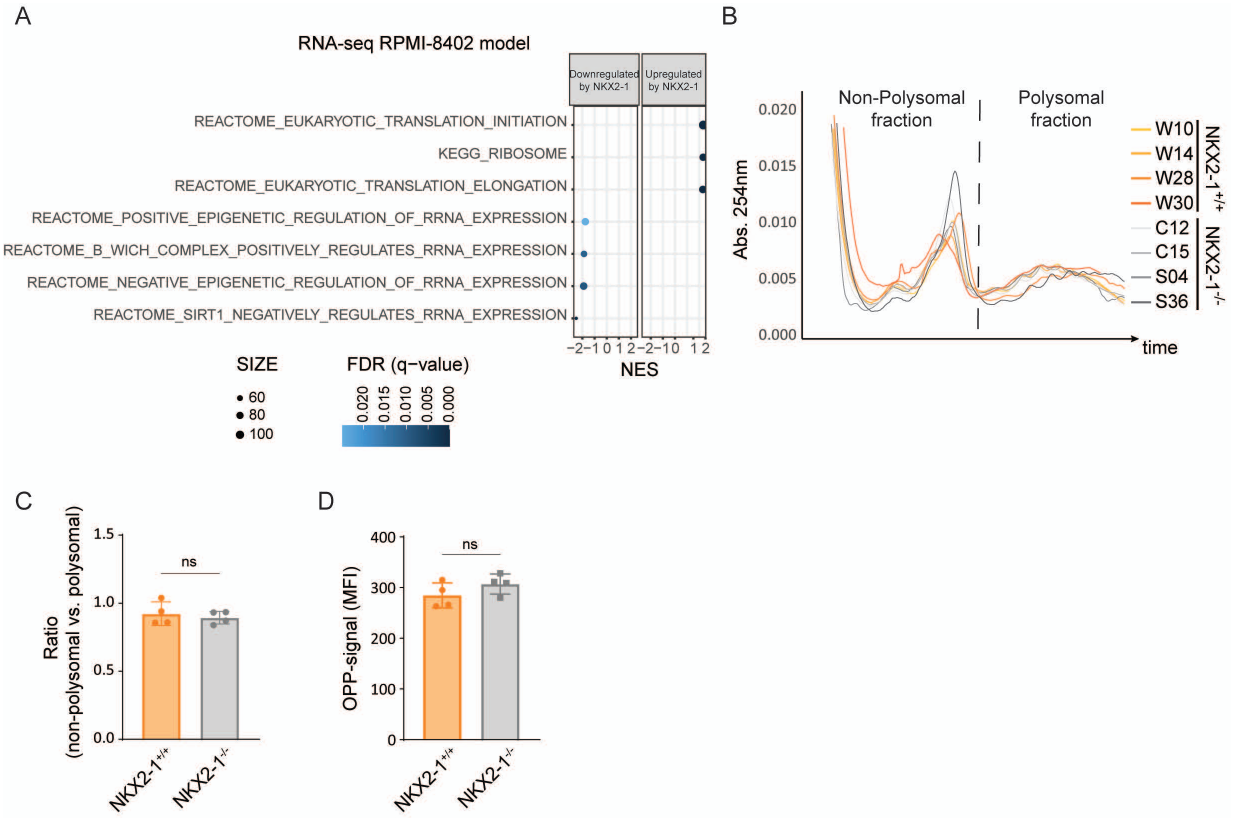

Figure S7. Ribosomal and translational characterization shows no major differences between NKX2-1$^{+/+}$ and NKX2-1$^{-/-}$ clones. (A) Dot plot showing enriched gene sets linked to ribosomes identified in the GSEA of differentially expressed RNA-seq genes in NKX2-1 RPMI-8402 clones. **(B)** Polysome profiles of NKX2-1$^{+/+}$ and NKX2-1$^{-/-}$ clones representing the 254 nm absorbance measured over time. The non-polysomal and polysomal fractions are delimited by the dotted line. **(C)** Ratio between area under the curve of the non-polysomal vs. polysomal fraction in NKX2-1$^{+/+}$ and NKX2-1$^{-/-}$ clones. **(D)** Mean Fluorescent Intensity (MFI) of OPP-positive cells measured by flow cytometry in NKX2-1$^{+/+}$ and NKX2-1$^{-/-}$ clones after OPP treatment for 60 min. Data in panel C and D are represented as mean ± SD. Individual dots represent 4 biologically independent clones per genotype. p-values were calculated using an unpaired two-tailed t-test. Individual dots represent the 4 biologically independent clones per genotype.

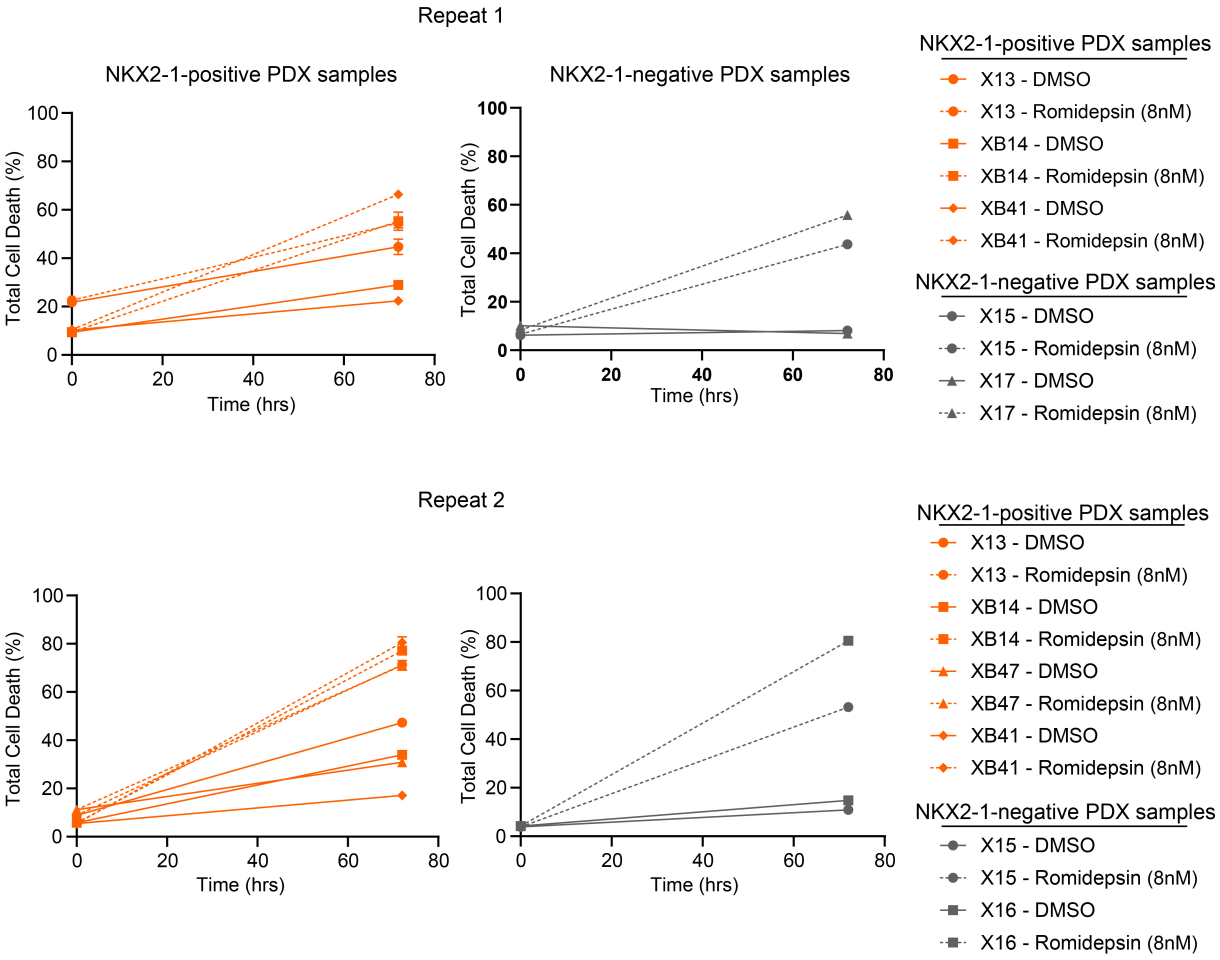

Figure S8. Cell death induced in PDX samples treated with Romidepsin. Total cell death of NKX2-1-positive and NKX2-1-negative PDX samples after Romidepsin treatment for 72 hours. Percentages of dead cells were determined as PI-positive staining cells in flow cytometry.

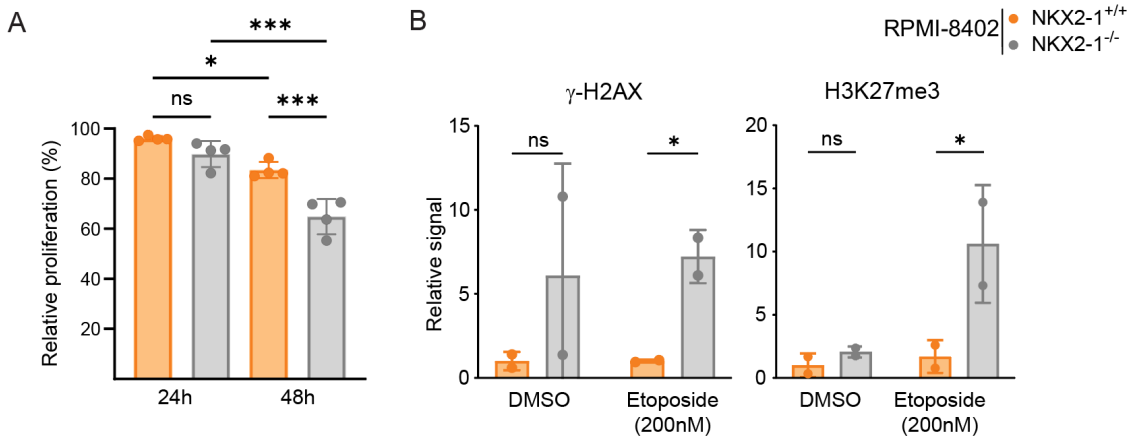

Figure S9. Etoposide effect on NKX2-1 RPMI-8402 model. (A) Relative viability of NKX2-1$^{+/+}$ and NKX2-1$^{-/-}$ RPMI-8402 clones after treatment with Etoposide for 24 and 48 h. Data are normalized to Day 0 and to the DMSO vehicle condition. Data represented as mean ± SD, statistics calculated by an ordinary one-way ANOVA followed by a Tukey's HSD post hoc test. **(B)** Quantification of γ-H2AX (left) and H3K27me3 (right) protein expression by western blotting from two independent experiments combining 4 biologically independent clones per genotype (blots shown in Figure 4C).

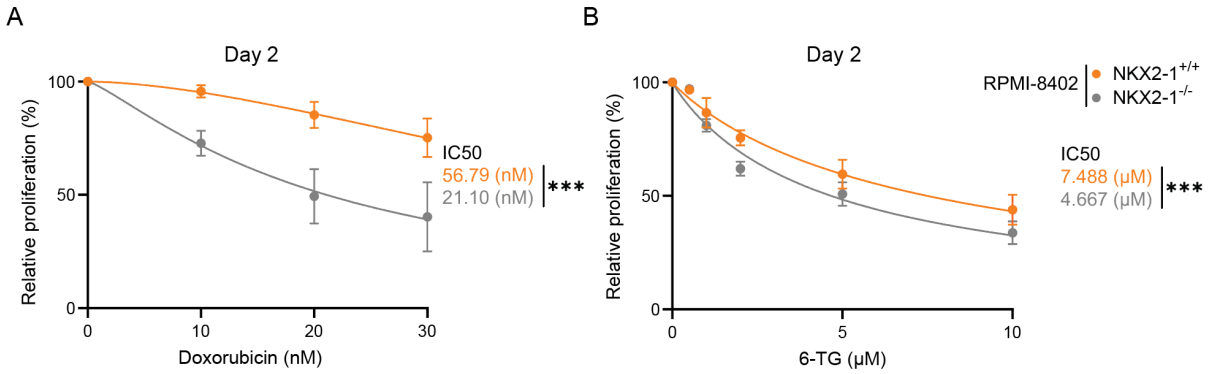

Figure S10. DNA-damaging agents dose response curves for NKX2-1 RPMI-8402 model. Dose-response curves of NKX2-1$^{+/+}$ and NKX2-1$^{-/-}$ RPMI-8402 clones treated for 48 h with Doxorubicin (left) or 6-TG (thioguanine) (right). Data points represent mean ± SD of relative proliferation, normalized to Day 0 and DMSO condition. Least-squares regression fits to the mean are shown (solid lines), and IC50 values were determined for each drug and condition. Statistics were calculated by an extra sum-of-squares F-test. ***p-value < 0.001.

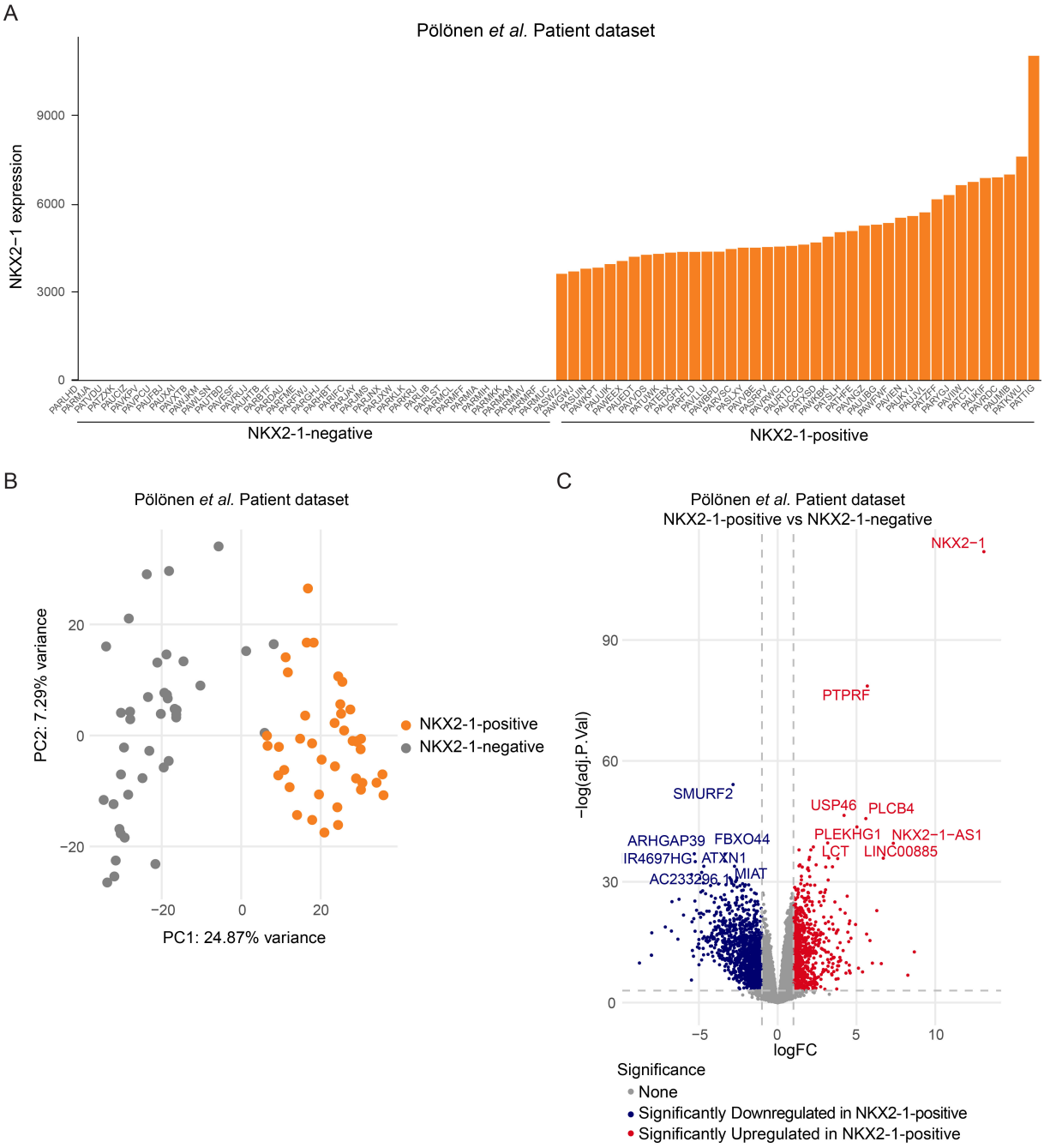

Figure S11. Description of RNA-seq T-ALL Patient dataset of Pölönen *et al.* [13] **(A)** NKX2-1 mRNA expression in 40 NKX2-1-negative TAL1 and 40 NKX2-1-positive T-ALL samples. **(B)** PCA plot showing the variation among the RNA-sequencing samples based on normalized expression data on NKX2-1-negative (grey) and NKX2-1-positive (orange) T-ALL samples. **(C)** Volcano plot showing differentially expressed genes between NKX2-1-positive and NKX2-1-negative T-ALL samples. The grey-dotted lines indicate the cut-off values for significance (adj.P.Val<0.05) and fold change (FC>2).

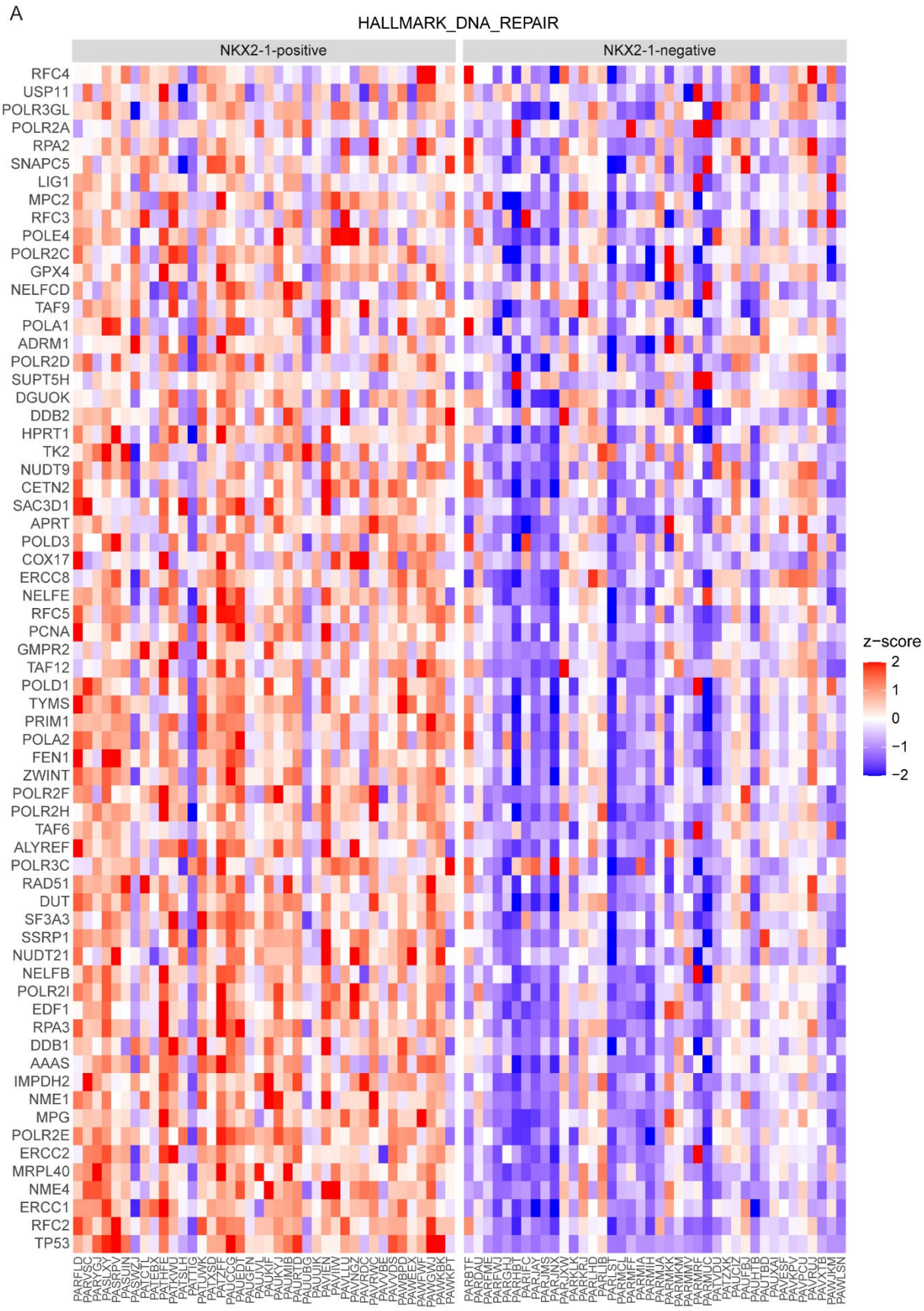
A
HALLMARK_DNA_REPAIR
NKX2-1-positive
NKX2-1-negative
RFC4
USP11
POLR3GL
POLR2A
RPA2
SNAPC5
LIG1
MPC2
RFC3
POLE4
POLR2C
GPX4
NELFCD
TAF9
POLA1
ADRM1
POLR2D
SUPT5H
DGUOK
DDB2
HPRT1
TK2
NUDT9
CETN2
SAC3D1
APRT
POLD3
COX17
ERCC8
NELFE
RFC5
PCNA
GMPR2
TAF12
POLD1
TYMS
PRIM1
POLA2
FEN1
ZWINT
POLR2F
POLR2H
TAF6
ALYREF
POLR3C
RAD51
DUT
SF3A3
SSRP1
NUDT21
NELFB
POLR2I
EDF1
RPA3
DDB1
AAAS
IMPDH2
NME1
MPG
POLR2E
ERCC2
MRPL40
NME4
ERCC1
RFC2
TP53
z−score
2
1
0
−1
−2

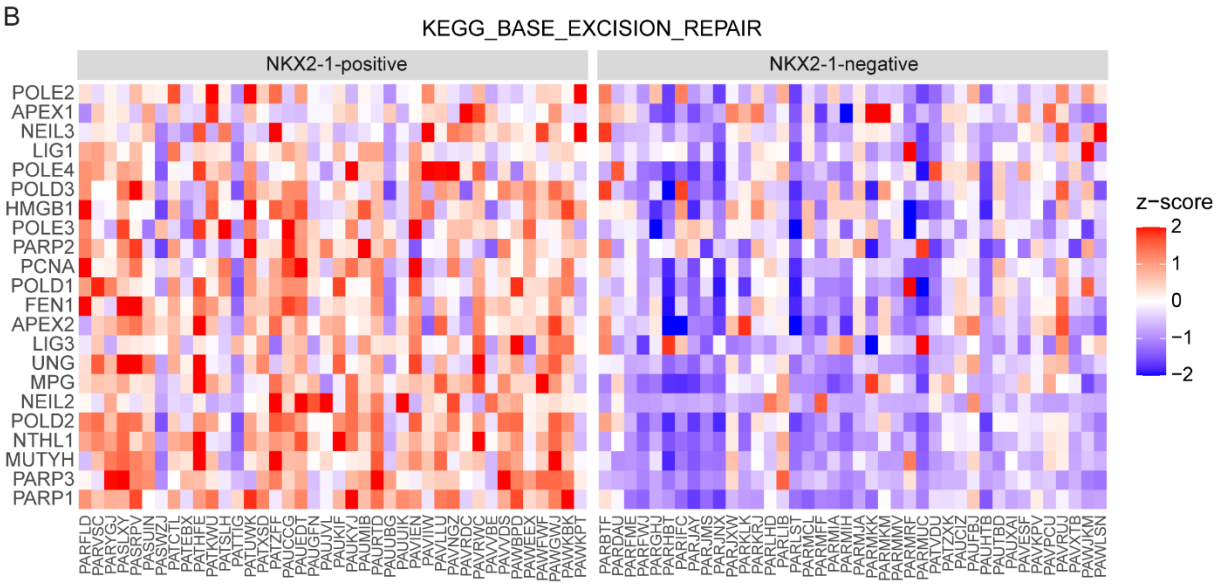

Figure S12. Heatmaps of DNA damage repair related GSEA pathways from Pölönen *et al*. (A-B) Heatmap showing expression of the leading-edge genes in NKX2-1 positive and NKX2-1 negative T-ALL samples of genes in the HALLMARK pathway "DNA_REPAIR" (A) and KEGG pathway "BASE_EXCISION_REPAIR" (B). Expression is shown as mean z-score.

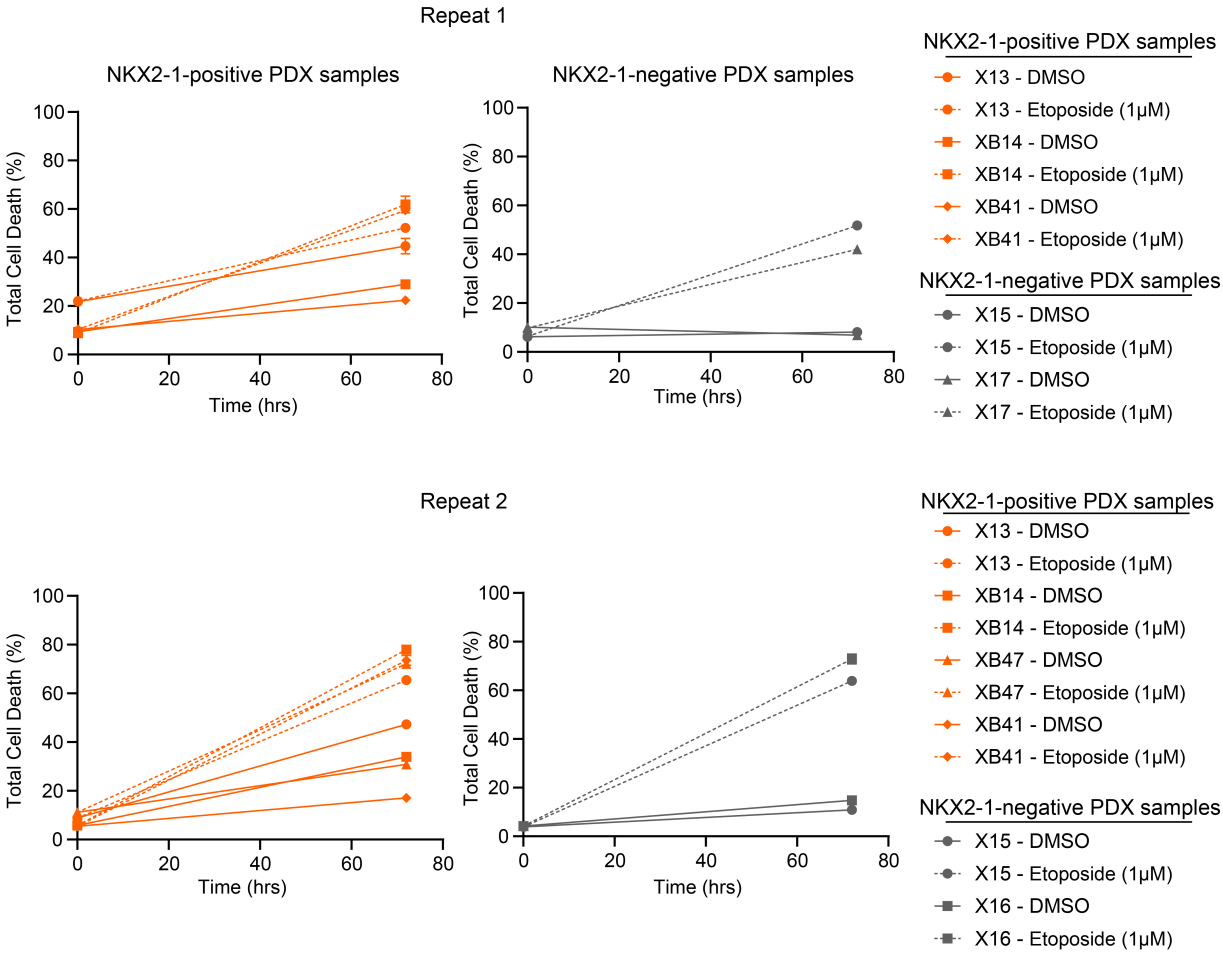

Figure S13. Cell death induced in PDX samples treated with Etoposide. Total cell death of NKX2-1 positive and NKX2-1 negative PDX samples after Etoposide treatment for 72 h. Percentages of dead cells were determined as PI-positive staining cells in flow cytometry.

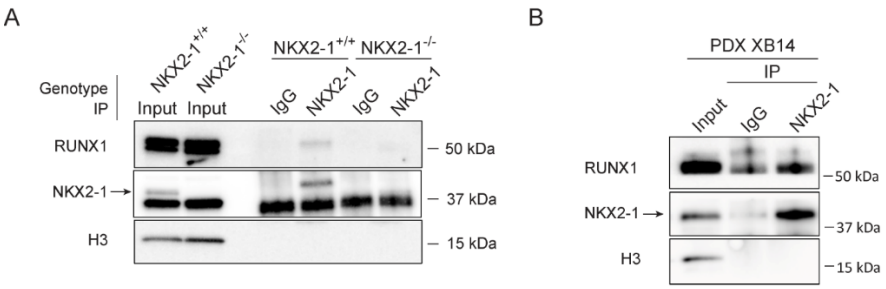

Figure S14. NKX2-1 co-immunoprecipitates with RUNX1 in T-ALL models. (A-B) Immunoblot for RUNX1, NKX2-1 and histone 3 (H3) of input, IgG control and NKX2-1 immunoprecipitated samples of NKX2-1$^{+/+}$ or NKX2-1$^{-/-}$ mixed RPMI-8402 clones (A) or NKX2-1-positive PDX XB14 (B).

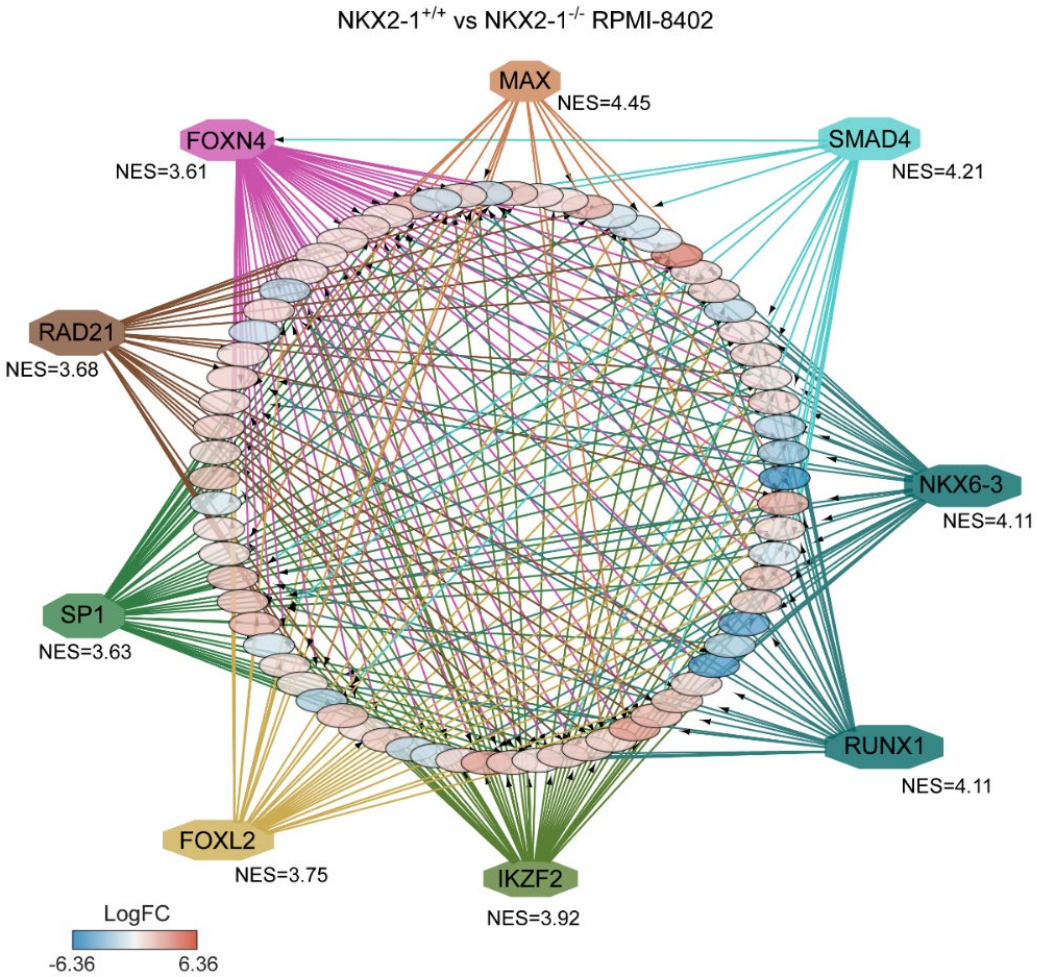

Figure S15. Network representation of transcriptionally regulated genes in RPMI-8402 model. iRegulon analysis on significantly differentially expressed genes (DEGs) in NKX2-1$^{+/+}$ clones compared to NKX2-1$^{-/-}$ clones. Representative transcription factors from 8 top scoring predicted clusters are indicated in the outside octagons. NES values for each cluster code are shown from each transcription factor. DEGs are colored according to their logFC.

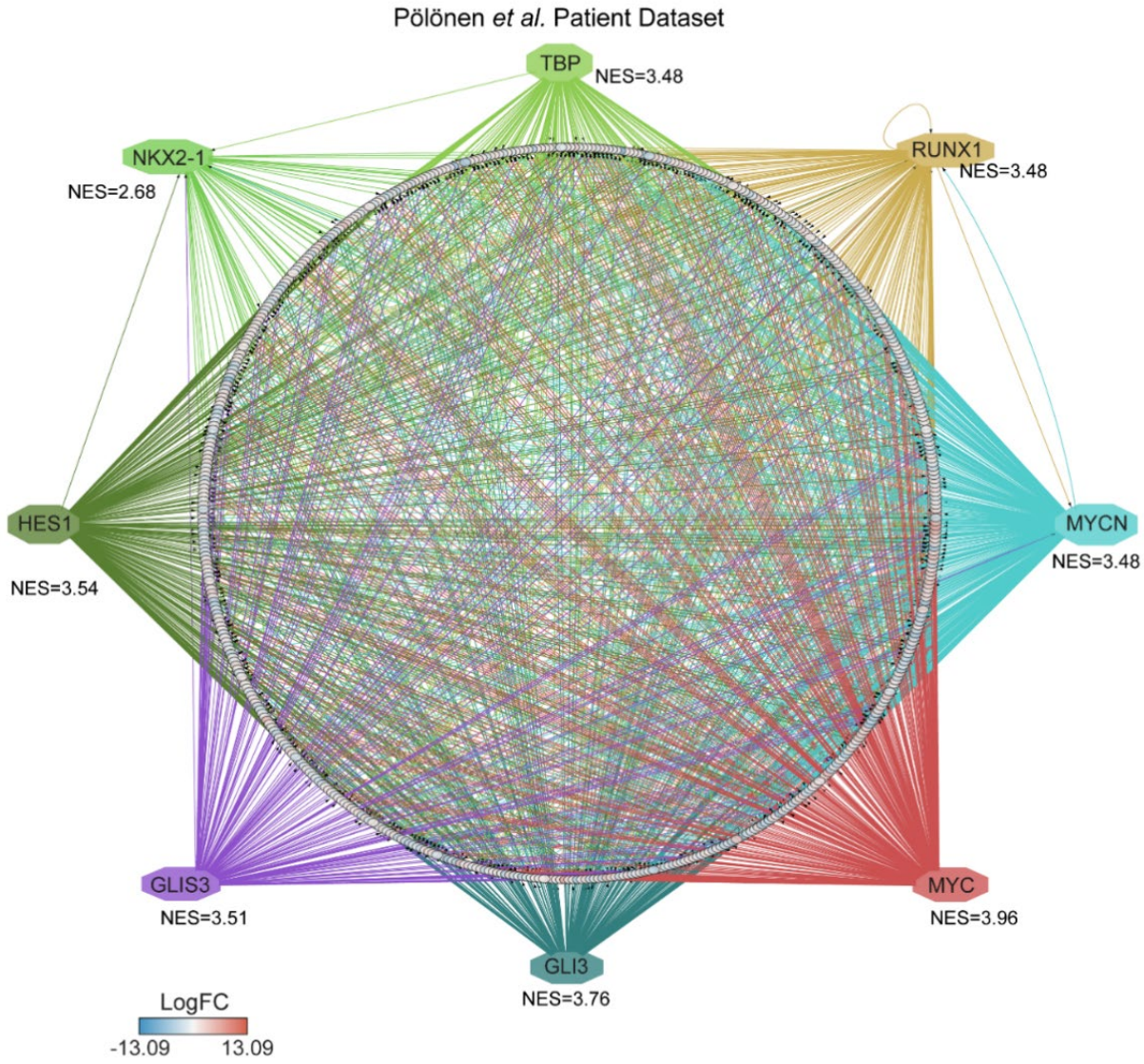

Figure S16. Network representation of transcriptionally regulated genes by NKX2-1 and RUNX1 in public T-ALL RNA-seq patient dataset. iRegulon analysis on top 10% significantly DEGs in NKX2-1 positive versus NKX2-1 negative T-ALL samples. Representative transcription factors from eight top scoring predicted clusters are indicated in the outside octagons. NES values for each cluster code are shown from each transcription factor.

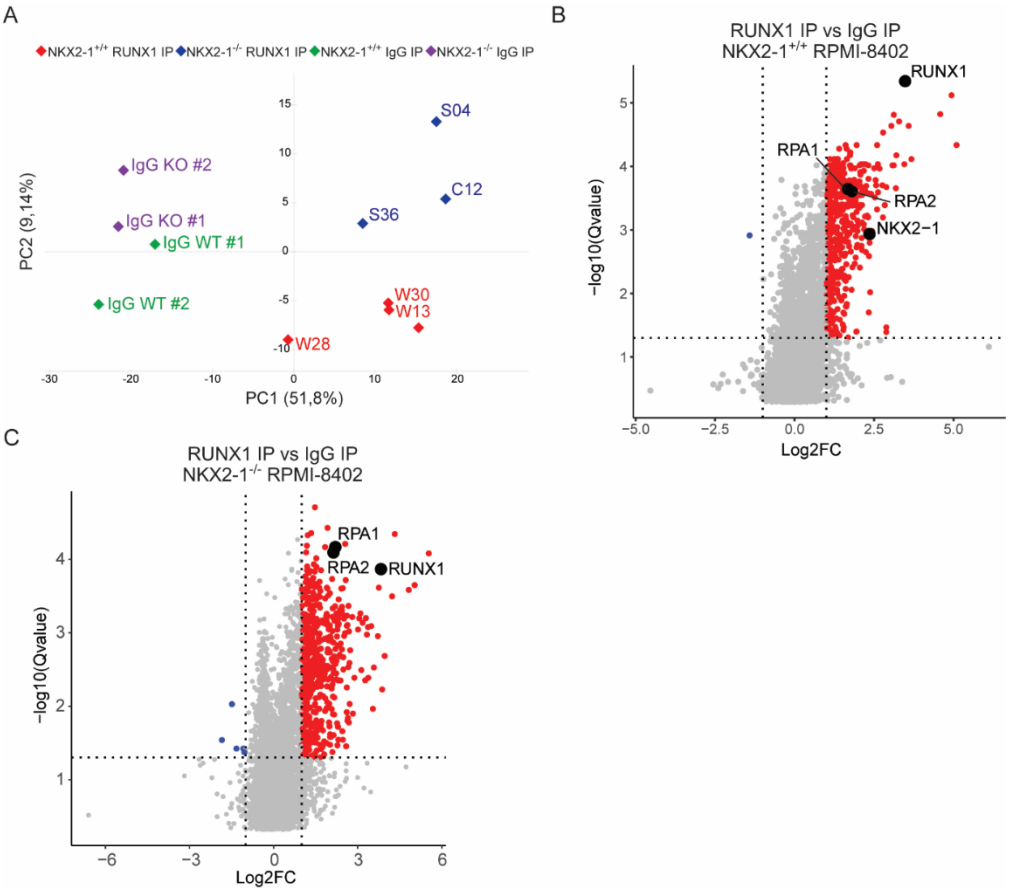

Figure S17. RUNX1 IP-MS in NKX2-1$^{+/+}$ and NKX2-1$^{-/-}$ clones. (A) PCA plot of RUNX1 and IgG IP-MS in NKX2-1$^{+/+}$ and NKX2-1$^{-/-}$ RPMI-8402 clones. **(B-C)** Volcano plot showing differentially detected RUNX1 binding proteins by IP-MS in NKX2-1$^{+/+}$ (B) or NKX2-1$^{-/-}$ (C) compared to IgG of each genotype. The grey-dotted lines indicate the cut-off values for significance (Qvalue<0.05) and fold change (FC>2).

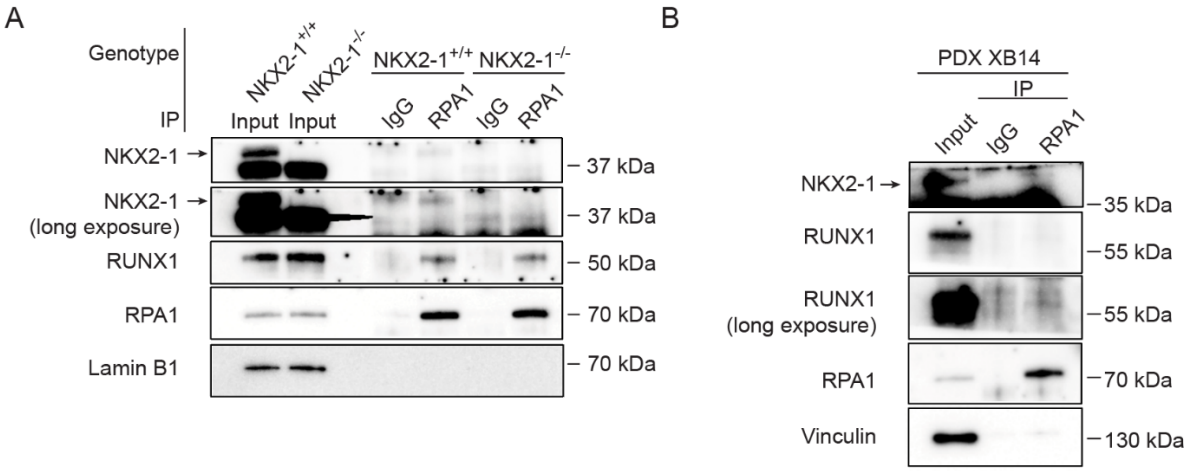

Figure S18. RPA1 co-immunoprecipitates with NKX2-1 and RUNX1 in T-ALL models. (A-B) Immunoblot for NKX2-1, RUNX1 (short and long exposure), RPA1 and Lamin B1 or Vinculin of input, IgG control and NKX2-1 immunoprecipitated samples of NKX2-1$^{+/+}$ or NKX2-1$^{-/-}$ mixed RPMI-8402 clones (A) or NKX2-1-positive PDX XB14 (C).

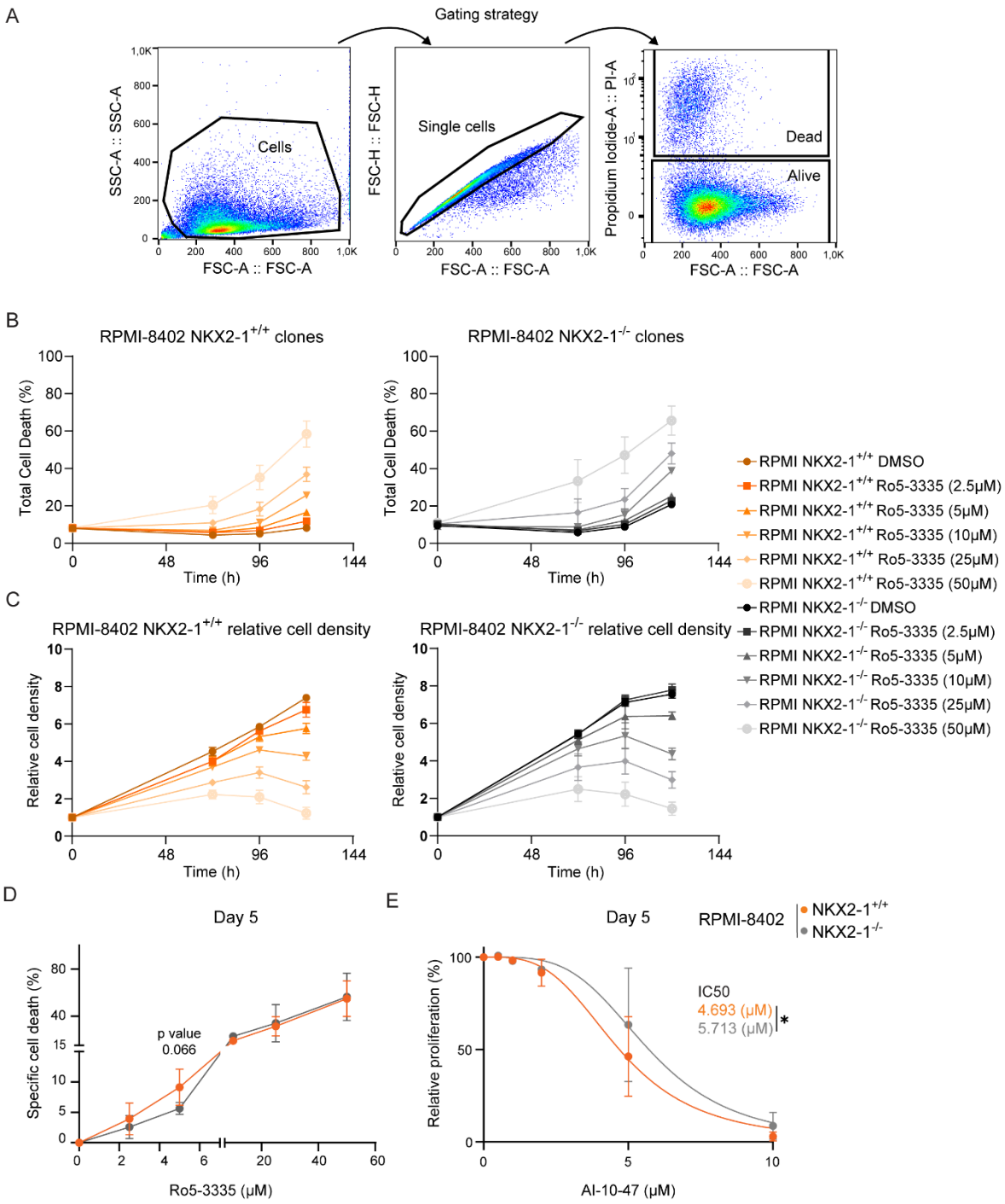

Figure S19. NKX2-1 enhances the sensitivity to pharmacological inhibition of RUNX1 in the RPMI-8402 model. **(A)** Gating strategy for cell viability using PI by flow cytometry. **(B)** Total cell death of NKX2-1$^{+/+}$ and NKX2-1$^{-/-}$ cells after Ro5-3335 treatment for 5 days. Dead cell percentages were determined as PI-positive cells in flow cytometry. **(C)** Proliferation curve of NKX2-1$^{+/+}$ and NKX2-1$^{-/-}$ cells after Ro5-3335 treatment over 5 days. Viable cell numbers plotted are PI-negative staining cells in flow cytometry. **(D)** Specific cell death on NKX2-1$^{+/+}$ and NKX2-1$^{-/-}$ RPMI-8402 cells treated for 5 days with the indicated concentrations of Ro5-3335. Specific cell death calculations were based on PI staining according to the formula specified in the supplementary materials and methods. Data represented as mean ± SD, statistics calculated by an unpaired two-tailed t-test. **(E)** Dose-response curves of NKX2-1$^{+/+}$ and NKX2-1$^{-/-}$ RPMI-8402 clones treated for 120 h with AI-10-47. Data points represent mean ± SD of relative proliferation, normalized to Day 0 and DMSO condition. Least-squares regression fits to the mean are shown (solid lines), and IC50 values were determined for each drug and condition. Statistics were calculated by an extra sum-of-squares F-test. Data in B, C, D and E are represented as

line graphs indicating the average value obtained for four independent clones per genotype, and the error bars indicate the SD on these measurements. *p-value < 0.05.

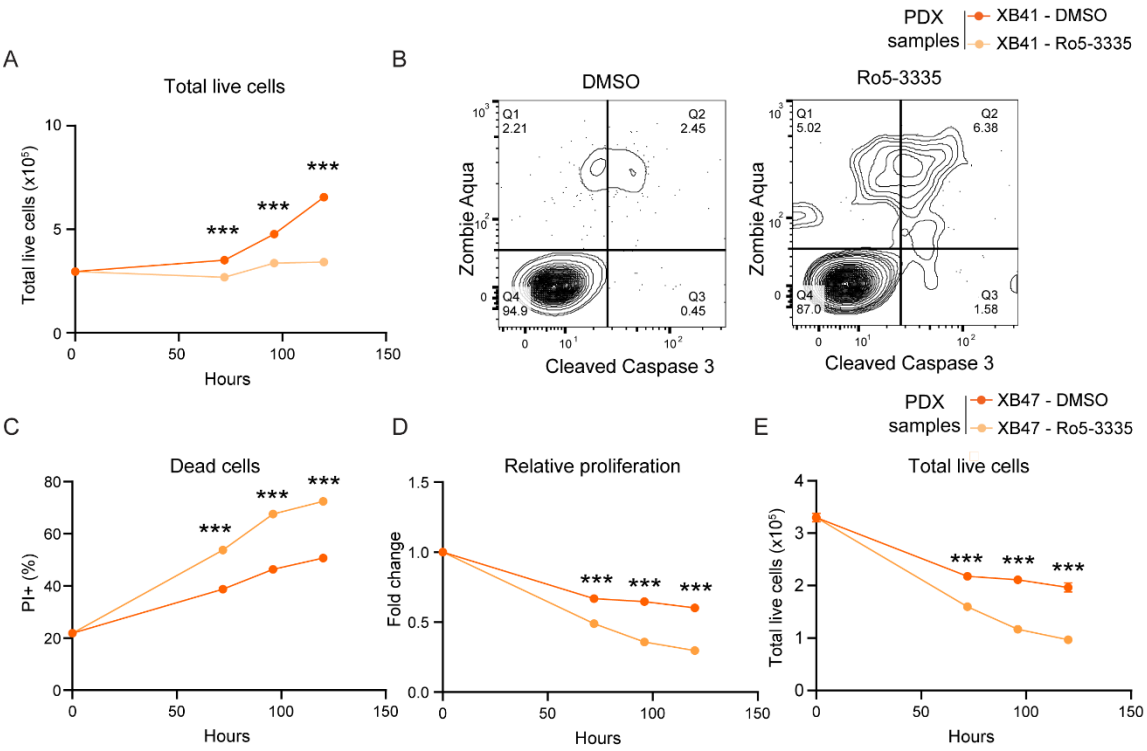

Figure S20. Effect of Ro5-3335 on two *ex vivo* cultured NKX2-1 positive T-ALL PDX samples. Effect of treatment of NKX2-1 positive PDX samples XB41 (top) and XB47 (bottom) with 50 µM Ro5-3335 or DMSO vehicle. **(A)** Total live cells during treatment. **(B)** Flow cytometry analysis of cleaved caspase 3/Zombie Aqua of NKX2-1 positive after 120 h of treatment. **(C)** Relative proliferation of treated XB47 cells normalized to Day 0. **(D)** Absolute percentage of dead cells, identified as PI positive cells by flow cytometry, during treatment. **(E)** Total live cells during treatment. Data in A, C, D and E are represented as mean ± SD of 3 technical replicates, statistics calculated by two-way ANOVA followed by a Šidák test. ***p-value < 0.001.

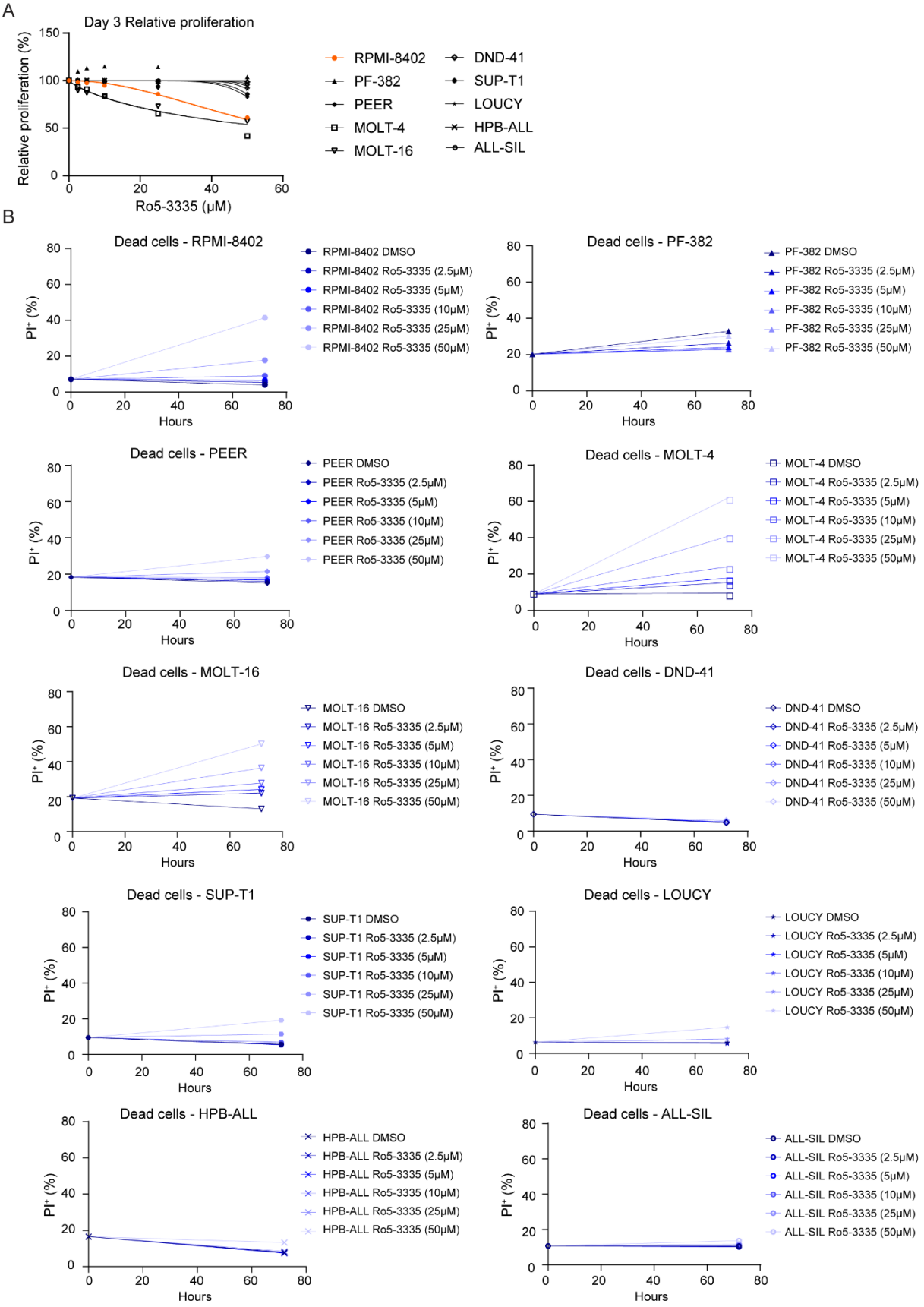

Figure S21. Ro5-3335 response of a panel of human T-ALL cell lines. (A) Dose-response curves of T-ALL cell lines treated for 72 h with Ro5-3335. Data points represent mean ± SD of relative proliferation, normalized to Day 0 and DMSO condition. Least-squares regression fits to the mean are shown (solid lines). The NKX2-1

positive RPMI-8402 cell line was included in the panel and indicated in orange. **(B)** Total cell death of T-ALL cell lines after Ro5-3335 treatment for 72 h. Percentages of dead cells were determined as PI positive cells in flow cytometry.